2023

Part Design Geometry-Driven toolpath Optimization for Additive Manufacturing Energy Sustainability Improvement

David Kolawole Somade
kolsomad2010@yahoo.com

ABSTRACT

PART DESIGN GEOMETRY-DRIVEN TOOLPATH OPTIMIZATION FOR ADDITIVE MANUFACTURING ENERGY SUSTAINABILITY IMPROVEMENT

David Kolawole Somade, MS
Department of Industrial and Systems Engineering
Northern Illinois University, 2023
Niechen Chen, Director

One of the most promising new manufacturing technologies in the past three decades is additive manufacturing (AM), also commonly known as three-dimensional (3D) printing or rapid prototyping. The energy consumption problem in AM can be significant when it is adopted at the industrial scale or used under resource-restricted conditions. The energy consumption of an AM process is influenced by several factors including bed heating, filament extrusion, material infill, component cooling, etc. All these factors are further determined by the equipment and the toolpath for a specific printing task. Build orientation and tool-path direction are frequently used to optimize part and process attributes; however, more in-depth research is required to determine how tool-path pattern choice affects the energy attributes of an AM process. The goal of this work is to develop a toolpath creation strategy for AM tasks under limited energy supply conditions. In AM process, due to factors like motor axis acceleration/deceleration and the total number and length of line segments on a path, the toolpath will have an impact on the amount of energy used to perform the printing task. We will approach our research goal by first developing a model that computes the energy consumption of an AM process based on the toolpath, then analyzing the impacts of part design geometry on the toolpath generation, and finally, creating a strategy to guide the generation of toolpath for specific part geometry to control the total energy requirement.

NORTHERN ILLINOIS UNIVERSITY
DEKALB, ILLINOIS

MAY 2023

PART DESIGN GEOMETRY-DRIVEN TOOLPATH OPTIMIZATION FOR ADDITIVE MANUFACTURING ENERGY SUSTAINABILITY IMPROVEMENT

BY

DAVID KOLAWOLE SOMADE

A THESIS SUBMITTED TO THE GRADUATE SCHOOL

IN PARTIAL FULFILLMENT OF THE REQUIREMENTS

FOR THE DEGREE

MASTER OF SCIENCE

DEPARTMENT OF INDUSTRIAL AND SYSTEMS ENGINEERING

Thesis Director:
Niechen Chen

TABLE OF CONTENTS

LIST OF TABLES

Page

LIST OF FIGURES

LIST OF APPENDICES

CHAPTER 1
INTRODUCTION

The term "Additive Manufacturing (AM)", also widely known as 3D printing (these two terms are mixed used in this work), refers to the method of fabricating three-dimensional objects by computer-numerically-controlled depositing/ curing/ sintering/ melting-solidifying materials, typically in layers. According to Jerry et al. (2017), Additive Manufacturing (AM) is becoming the dominant next-generation manufacturing method and is significantly transforming numerous industries such as transportation, biomedical, sports, automotive, and aerospace.

This novel manufacturing process presents advantages over conventional manufacturing processes in terms of the capability to generate physical objects in extraordinarily complex geometry with lower cost and shorter product realization time. According to Ong et al. (2008), Additive Manufacturing (AM) was initially developed as a set of technologies for rapid prototyping. The rapid growth of the AM market is attributed to its unique advantages over traditional manufacturing techniques. One of the major benefits of AM over conventional methods is its capability to produce complex geometries. Tuck et al. (2008) summarized two advantages of AM over traditional manufacturing processes. Firstly, AM allows for the creation of components without many of the geometric constraints that apply to conventional manufacturing methods such as formation and subtraction. Secondly, AM makes it possible to produce small quantities of potentially customized products at a relatively low unit cost. Warburg (2018) further mentioned manufacturing cost reduction, less material waste, part assembly stage elimination, and product customization as important functional differences between AM and other manufacturing methods.

The Additive Manufacturing (AM) machinery industry has exhibited significant growth potential in the last decade. Formlabs (2022) reports that the 3D printing market generated $6 billion in sales in 2017 and is predicted to grow at a compound annual rate of 30.2% to achieve a total market size of $22 billion by 2022. Wohlers (2016) also projected that the global 3D printing-related sectors would reach a market size of $20.2 billion by 2021. Consequently, AM has the potential to revolutionize the way products are designed, produced, and marketed. As costs continue to decrease, additive manufacturing is expected to become more prevalent in traditional consumer products (Formlabs, 2022). Li et al. (2017) provided an example of affordable desktop 3D printers costing less than $5,000, which are now routinely used in homes, offices, libraries, and labs due to recent advancements that have made them more accessible.

Despite the recent advancements in Additive Manufacturing (AM), the current technology still has a few limitations that hinder its extensive use in large-scale industrial production. Ruffo and Hague (2007) identified some of these constraints, including material selection, process productivity, product dimensional accuracy, surface quality, repeatability, and energy consumption. In terms of energy consumption, Ajay et al. (2017) found that it could constitute up to 32% of the total cost of 3D printing, highlighting the pressing need for an energy optimization approach for 3D printers.

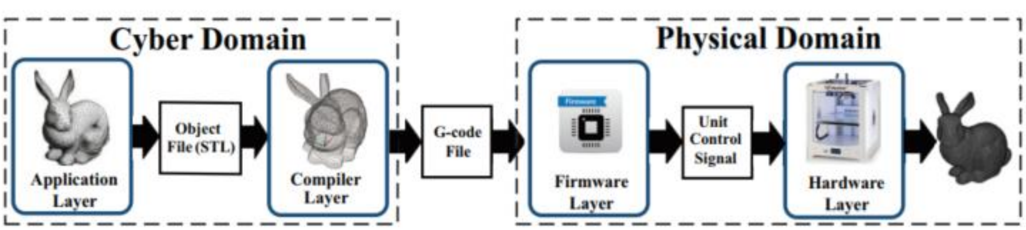

Figure 1. 3D printing flowchart (Ajay et al., 2017, p. 2).

There are various functional entities that contribute to the 3D printing stages as described by Ajay et al. (2017). They include:

- **Application:** Under this layer, the 3D model design is created in a Stereolithography format (STL) by computer-aided design (CAD) software (e.g., SOLIDWORKS, Siemens NX, Autodesk Inventor, etc.).
- **Slicer:** This generates a toolpath file from the STL file which is called a G-code file. A sequence of instructions that control the printing process is contained in the G-code file.
- **Firmware:** The 3D printer's firmware decodes the G-code file and produces the necessary control signals for the hardware.
- **Hardware:** This is the physical component of a 3D printer that carries out the printing tasks based on control signals from the firmware. For a Fused Deposition Modelling (FDM) printer, these include the stepper motors, cooling fans, and heater. Figure 2 describes the hardware component of an FDM printer.

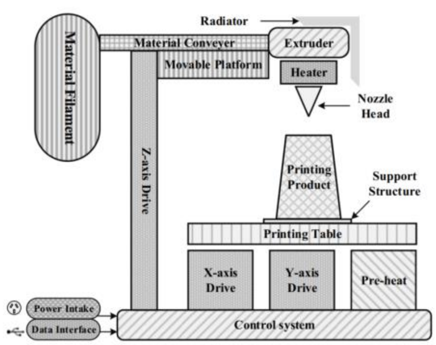

Figure 2. FDM printer hardware components (Peng, Analysis of energy utilization in 3D printing processes, 2016, p. 2).

The typical toolpath for 3D printing consists of a "shell" boundary and an infill lattice, which is usually a standard mesh. The infill lattice is generated using common patterns like rectilinear, grid, triangles, and stars, among others. To print the part layer by layer in a specific build direction, a G-code file includes the necessary process parameters and toolpath information.

The energy consumed during a 3D printing task is mainly attributed to the power required to operate the hardware components based on the toolpath created for the task (Fysikopoulos et al., 2013). While the toolpath determines the motion of all axes, existing planning strategies primarily focus on time, material, and part quality, with little attention to energy consumption. Consequently, current practices may result in unnecessary power usage for a given 3D printing task. Therefore, there is significant potential for innovation in toolpath planning strategies to optimize power consumption during 3D printing.

This research aims to answer two key questions about the energy efficiency of 3D printers:

1. Does the toolpath pattern contribute to the energy consumption of a printing operation? How significant is this?
2. How can we plan the toolpath generation process based on the design geometry of the part to minimize energy usage?

To achieve this, an analysis of the energy consumption of the printer hardware components will be conducted based on the layer geometry and toolpath. Subsequently, a strategy will be developed to ensure the generation of an optimal toolpath for each geometry on a layer-by-layer basis. This optimal toolpath planning which entails Toolpath type and geometry matching through angle orientation and analysis will be done smartly and can contain a hybrid of toolpath pattern types rather than the conventional approach of "one pattern fit all" strategy.

Objectives and Scope

The objective of this research is to develop a toolpath planning strategy for additive manufacturing (AM) tasks under limited energy supply conditions. Out of all available AM technologies, this research focuses on material extrusion-based 3D printing (e.g., FDM), which extrudes melted plastic out of a nozzle to deposit in beads that fuse together upon contact and follow a predefined toolpath.

CHAPTER 2
LITERATURE REVIEW

This study aims to better understand the techniques used to analyze layer-level geometry required for 3d printing, various toolpath planning and optimization techniques in AM, energy consumption methods, and approaches for driving sustainability in AM.

Recent research on energy consumption in AM can be organized under the following broad categories:

1. Sustainability factors in AM
2. Energy Consumption Analysis for AM Systems
3. Geometry Analysis in AM
4. Toolpath Planning and Optimization in AM

Table 1 shows a summary of the literature collected on the four categories as part of this project, and the collected sources are discussed briefly in the following sections.

Sustainability factors in AM

According to Sikdar (2003), the major goal of a sustainability study in a manufacturing process is to limit the use of resources and non-renewable energy which can be illustrated in Figure 3. Additive manufacturing (AM) offers several sustainability advantages, including geometry optimization that helps in reducing material and energy consumption, decreased waste generation, lower logistics requirements in the supply chain, and reduced inventory waste due to Just-in-Time spare part production (Chen et al., 2015).

In their investigation of AM adoption, Ford and Despeisse (2016) utilized a life cycle perspective. They found that sustainability benefits can be achieved in four significant areas, which include product and process redesign, material input processing, make-to-order product manufacturing, and closing the loop. Drizo and Pegna (2006) carried out an extensive environmental impact assessment study of current additive technologies, using multifunctional measurement and evaluation methodologies. Their findings revealed that Rapid Prototyping (RP) and Rapid Tooling (RT) technologies have the potential to revolutionize design and manufacturing. Kellens et al. (2012) put forward a systematic Life Cycle Inventory (LCI) data collection approach to address the limitations that can arise from the quantitative analysis of environmental impact studies. Their research concluded that the build height and volume have an impact on energy consumption (Kellens et al., 2014).

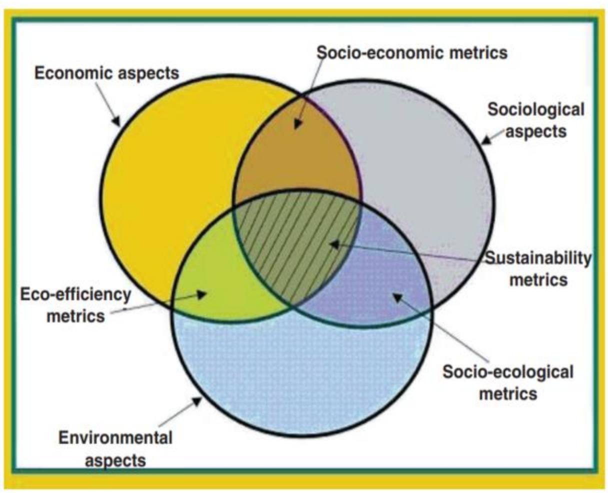

Figure 3. Sustainability development model (Azapagic and Perdan, 2000, p.244).

Sreenivasan et al. (2009) conducted a sustainability analysis on Selective Layer Sintering (SLS) procedures and computed four energy segments based on components. They documented the energy usage of roller drives (25%), stepper motors (25%), chamber heaters (36%), and laser transmitters (16%). In their study, they suggested creating a better heat management system or using an energy-efficient laser transmitter to reduce energy consumption (Sreenivasan et al., 2010). After developing an energy consumption model for a Binder Jet AM process, Meteyer et al. (2014) recognized the need to assess the environmental impact of material production and disposal to perform a complete Life Cycle Assessment. Santos et al. (2012) evaluated energy consumption in an FDM system for three types of interior component fills: Solid, Sparse High Density, and Sparse Low Density. They also developed a computational tool for decision-making that incorporates eco-design concepts to gather information on a product's environmental impact at each step of its life cycle.

The environmental analysis of 3D printing processes was determined using the analytical approach proposed by Munoz and Sheng (1995) for cutting technologies. Figure 4 shows the three dimensions of their analysis, which are Energy, Material, and Time.

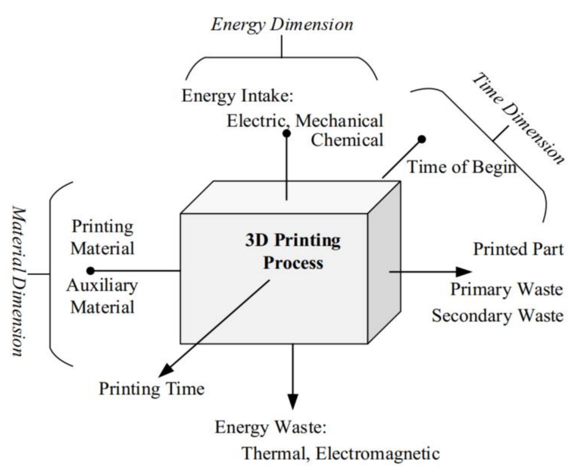

Figure 4. Various dimensions of environmental analysis in a manufacturing process (Munoz and Sheng, 1995, p. 739).

In addition to the technical studies mentioned earlier, the adoption of AM technologies has also been assessed for its social effects, as highlighted by Huang et al. (2013). Baumers et al. (2016) and Weller et al. (2015) have explored future challenges, economic analysis, and occupational risks associated with the use of AM technologies. Huang et al. (2013) identified three main areas of research on the effects of AM technology, namely energy consumption and environmental impact, effects on physical health and well-being, and supply chain potential for manufacturing. The adoption of AM technology can contribute to a more sustainable industrial system by offering opportunities for environmentally friendly production and consumption (Ford and Despeisse, 2016). It is important to be mindful of energy usage in 3D printing and to identify energy-consuming components in line with the increasing emphasis on driving sustainability in manufacturing.

Energy Consumption Analysis for AM Systems

More academic research is needed to address the issue of energy consumption in AM processes, which is regarded as a significant factor that persists today (Drizo and Pegna, 2006; Short et al., 2015). May et al. (2013) emphasized that evaluating the energy use of a 3D printer is a prerequisite for assessing its printing capabilities and manufacturing sustainability. To address the gaps in the literature, they developed two frameworks that highlight the importance of KPIs in an overall energy management strategy. In addition, they provided guidance for a new methodology for developing KPIs.

Several academic studies have aimed to determine the energy consumption of various AM processes. For example, Sreenivasan and Bourell (2009) discovered that the chamber heater was responsible for most of the power consumption in the SLA system. Meteyer et al. (2014) examined the energy flow and consumption in a Binder Jet AM process and tested their model using three separate processes: printing, curing, and sintering. They also acknowledged that statistically controlled tests were necessary to validate their proposed model. In a comparative study of eight different manufacturing processes, including FDM, SLS, CNC machining, injection molding, and shaping, Weissman and Gupta (2011) found that the volume of the products significantly impacted the energy consumption of FDM and SLS.

Several studies have been conducted to model the energy consumption of AM processes and investigate the relationships between different factors and energy usage, in addition to those that measure and compare energy consumption. Mognol et al. (2006) explored the energy consumption of three AM systems, namely Thermojet, FDM, and direct metal laser sintering, and analyzed the effects of various factors such as build orientation, support design, layer thickness, and production time. The researchers found that reducing manufacturing time is crucial for minimizing energy consumption; however, they also concluded that there is no universal guideline for energy optimization. Strano et al. (2011) developed a computational model for enhancing the production of components manufactured by SLS. They incorporated process effectiveness and efficiency to create a method that reduces both surface roughness and energy usage at the same time. In another study, Paul and Anand (2012) established a mathematical model in which energy consumption was a function of the total sintering area and related to factors such as layer thickness, geometry, and build orientation. Nonetheless, their investigation only examined laser energy and did not consider other sources of energy consumption such as platform energy and heating energy. Baumers et al. (2011) published their findings on a comparison of the energy usage of two laser sintering systems. In their research, they classified energy into four categories: task, geometry, time, and Z-height. They found that the time-dependent component was the most significant contributor to energy consumption. Meanwhile, Walls et al. (2014) studied the power consumption of several low-cost 3D printers and confirmed that their energy requirements varied. Peng (2016), on the other hand, focused only on quantifying the energy consumption of 3D printers during the heating process, while other aspects were underexplored. Ajay et al. (2017) developed an instruction-level model to precisely measure the energy used during a 15-minute print. They discovered that the biggest power usage was in the motor components (51.7%) and concluded that reducing the working time of the motors could significantly decrease the energy usage in 3D printing. They also utilized a cross-layer energy optimization approach by dynamically power-gating the X and Y motors, resulting in a total energy reduction of 25%. Nguyen et al. (2021) discovered that stepper motors and heaters have the most significant impact on power consumption. They developed an optimization strategy based on temperature delivery by print area, which reduced power usage by up to 23%. Additionally, they noted that print time is a crucial factor that affects power consumption.

From the studies conducted, it is evident that several factors, including print time, heating components, motor drive, product volume, printing speed, and layer count, influence AM consumption across multiple printing technologies. The heating component consumes the most energy, and the axes motor is the next biggest factor. Much research work is on reducing heating component energy consumption by reducing the number of layers, printing time, and/or using an array of small heating elements. However, there is a need to investigate the motor component energy consumption whose operations are directly influenced by geometry and toolpath.

Geometry Analysis in AM

The optimization of geometry is a crucial factor that impacts the reduction of material and energy usage in additive manufacturing (AM), according to Chen et al. (2015). Franco et al. (2010) assessed the effect of energy density on two polymeric materials during linear sintered structure processing by examining the geometrical characteristics. Yang et al. (2015) investigated methods for designing geometry to improve AM printing and proposed a simple technique based on control points for constructing heterogeneous porous structures. Meanwhile, Baumers et al. (2016) conducted research on the relationship between geometric complexity and energy usage during Electron Beam Melting (EBM) procedures. They concluded that EBM did not display a significant correlation between form complexity and energy usage per layer. Kim et al. (2018) explored the effects of various printing factors on the line structure produced by FDM, including the thickness, breadth, and cross-sectional shapes of the extruded lines. They also created a model based on experimental findings to determine the optimal printing parameters for line creation. Sulaymon et al. (2022) utilized topology optimization techniques to redesign a bicycle seat model with a complex geometric structure, achieving a 50% reduction in material usage. Gardan and Schneider (2015) also used topology optimization in AM, developing an approach to maximize the interior component and complement the exterior skin of a part. They tested their technology with 10 distinct pieces using FDM, SLS, and SLA procedures. John et al. (2022) focused on cell geometry as a process factor to optimize the challenging 3D printing process and employed Taguchi design of experiments and Grey Rational Analysis to streamline the optimization.

Ribeiro et al. (2018) investigated the importance of interface design in multi-material 3D printing using fused filament technology. They found that multi-material prints intended for mechanical use require an interface geometry that is both more durable and macroscopic in nature. Similarly, Kakaraparthi et al. (2022) studied the mechanical properties of multi-material 3D printed objects by focusing on the interface zone formed at the geometric boundaries where different materials meet. They compared the mechanical performance of four different test samples and demonstrated the positive impact of inserting boundary interlock geometry, which resulted in improved tensile strength.

Existing research on AM part geometry design has primarily focused on improving component quality, with limited studies investigating the impact of part geometry design on energy usage in AM.

Toolpath Planning and Optimization in AM

There have been several studies focused on toolpath planning for AM printing. For instance, Ajay et al. (2017) significantly reduced energy consumption by analyzing the toolpath pattern's instruction movement. They used their findings to optimize the G-code to turn on/off stepper motors when detecting a straight line along the toolpath. In another study, Fleming et al. (2017) developed a greedy algorithm for post-processing toolpath instructions using a Traveling Salesperson Problem (TSP) solver to minimize the distance between subsequent space-filling curves and layers, thereby reducing unnecessary extrusion by at least 20% for their test models. Additionally, Gupta et al. (2020) built a framework that uses the Euler transformation to generate a new polygonal mesh representation of the sparse infill region of a layer-by-layer 3D printing operation. Their algorithm ensured the creation of a continuous toolpath covering the domain in every layer without any crossovers.

Several techniques have been proposed to minimize the toolpath length in 3D printing. One such technique by Wah et al. (2002) limits the total toolpath length within layers for a general layered manufacturing problem. Wojcik et al. (2015) use a genetic algorithm that combines raster toolpath segments to minimize the toolpath length for 3D printers. Volpato et al. (2014) propose two optimization-based techniques for reducing the overall route length of a 3D printed item by merging printed sections. Jin et al. (2014) proposed a method for eliminating pointless toolpaths by using parametric curves to connect sub-paths and avoid deceleration/acceleration processes in the starting and ending sections of sub-paths. The mechanical strength of the toolpath pattern has also been studied, with John et al. (2022) conducting tensile tests on six different patterns and finding that the square pattern exhibited the best tensile strength performance.

Based on the current literature, it can be concluded that energy consumption is a significant contributor to the recurring operating costs of AM machines, and further investigation is necessary to decrease the specific energy consumption of AM tasks. Although research on AM toolpath is primarily geared towards improving print quality and reducing material deposition, there is a need to extensively examine the impact of part geometry design on energy consumption in AM. While various AM technologies operate differently, the methodology for studying and optimizing energy consumption remains the same. In relation to our work, particular attention will be given to the most widely used and cost-effective AM technology, namely Fused Deposition Modelling (FDM).

Table 1. Summary of past literature reviewed.

Categories	Driving Sustainability	Energy Consumption Analysis	Geometry Analysis	Toolpath Planning	Proposed Research
Ajay et al. (2017)		X		X	
Baumers et al. (2011)		X			
Baumers et al. (2016)			X		
Chen et al. (2015)	X	X	X		
Drizo and Pegna (2006)	X	X			
Fleming, et al. (2017)				X	
Ford and Despeisse (2016)					
Franco et al. (2010)			X		
Gardan and Schneider (2015)			X		
Gupta et al. (2020)				X	
Huang et al. (2013)	X	X			
Jin et al. (2014)				X	
John et al. (2022)			X	X	
Kakaraparthia et al. (2022)			X		
Kellens et al. (2012)	X	X			

(Continued on following page)

Table 1 (continued). Summary of past literature reviewed.

Categories	Driving Sustainability	Energy Consumption Analysis	Geometry Analysis	Toolpath Planning	Proposed Research
Kim et al. (2018)			X		
May et al. (2013)					
Meteyer et al. (2014)		X			
Mognol et al. (2006)		X			
Munoz and Sheng, (1995)					
Nguyen et al., (2021)		X			
Paul and Anand (2012)		X			
Peng (2016)		X			
Peng and Yan (2018)			X		
Ribeiro et al. (2018)			X		
Santos et al. (2012)				X	
Short et al. (2015)		X			
Sikdar (2003)	X				
Sreenivasan et al. (2009)	X	X			
Sreenivasan et al. (2010)	X	X			
Strano et al. (2011)		X			
Sulaymon et al. (2022)			X		
Volpato et al. (2014)				X	
Wah et al. (2002)				X	
Walls et al. (2014)		X			
Weissman and Gupta (2011).		X			
Weller et al. (2015)	X				
Wojcik et al. (2015)				X	
Yang et al. (2015)			X		
Somade (2023)	X	X	X	X	X

CHAPTER 3

METHODOLOGY

A preliminary analysis was conducted to determine the power consumption of the heated bed, nozzle, and motor during the printing process. The analysis was carried out for a star geometry printing task with different toolpath patterns, namely Rectilinear, Hilbert curve, and Concentric. The results were consistent with existing literature and showed that stepper motors accounted for more than 33% of the overall power consumed during an average printing task of 30 minutes or more. Figure 6 shows that stepper motors are the second most significant factor after the heated bed. If heated bed is omitted, as many of the 5-axis or hybrid AM and machining machines do, then it can be inferred that the stepper motors would be the primary energy consumption factor in an FDM-AM process. To address the gap in existing literature, this research tackles the issue of energy consumption in the AM process by developing an accurate model to calculate energy usage based on the toolpath. This model was then used to analyze the impact of toolpath strategies on energy consumption for individual part design geometries. By conducting experiments, the optimal toolpath pattern type, toolpath orientation, and part geometry orientation were determined. Based on these findings, strategies to guide the generation of toolpath for specific part geometries were recommended to control the total energy requirement. The energy consumption model was built based on real-time power consumption data collected from each hardware component in a series of experiments using an open-source FDM 3D printer.

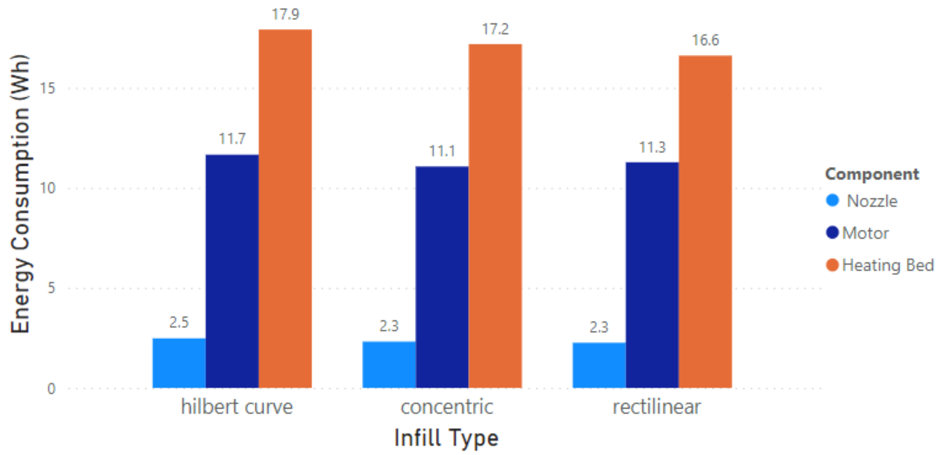

Figure 5. Energy density distribution for different toolpath pattern types

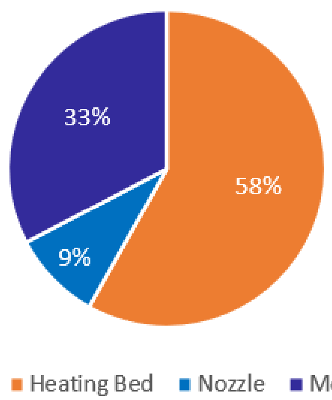

Figure 6. Components Power distribution for Hilbert curve toolpath in percentage

Component level energy consumption measurement

The accuracy of the energy data obtained from the 3D printer firmware was confirmed by cross-checking it against the energy readings displayed on a multimeter. A customized image recognition optical character recognition (OCR) Python script was used during several sample prints to accomplish this. To validate the approach, nine prints with varying geometries and toolpath patterns were utilized, and the results were summarized in Table 2. Additionally, the accuracy of the data extracted from the firmware is shown in the line graph presented in Figure 7. The results indicated that there was an average variance of 0.039% between the two sources, which was relatively small. Consequently, it was decided to proceed with using the energy data extracted from the firmware for the convenience of efficiently collecting energy consumption data.

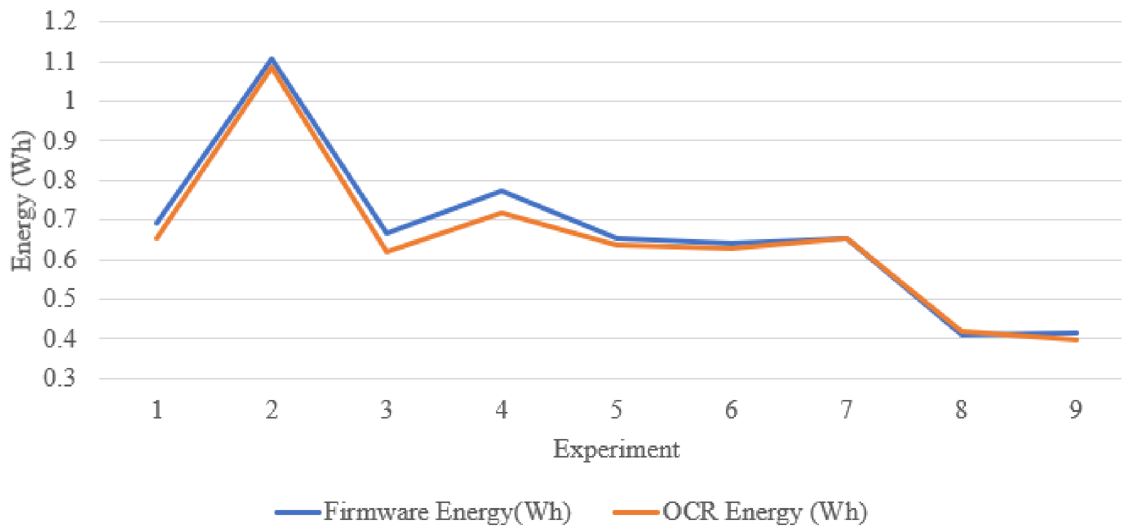

Figure 7. Line plot showing comparison between Firmware and Multimeter (OCR) Energy Consumption Captured in Watts-hour

.

Table 2. Validation of energy consumption information extracted from 3D printer.

#Exp	**Geometry**	**Toolpath pattern**	**Infill Angle**	**Firmware Energy (W-h)**	**OCR Energy (W-h)**	**Variance (%)**
1	Rectangle	Hilbert Curve	45	0.6909	0.6556	0.0539
2	I- shape	Hilbert Curve	45	1.1053	1.0845	0.0187
3	K-shape	Rectilinear	90	0.6681	0.6204	0.0770
4	L-shape	Archimedean Spiral	45	0.7756	0.7175	0.0810
5	L-shape	Concentric	90	0.654	0.6353	0.0294
6	L-shape	Rectilinear	0	0.6411	0.6294	0.0186
7	L-shape	Rectilinear	90	0.6545	0.6519	0.0039
8	R-shape	Rectilinear	0	0.4089	0.4175	0.0204
9	R-shape	Rectilinear	45	0.4165	0.3974	0.0482
					Average	**0.0390**

Mathematical energy consumption estimation model

A mathematical model was developed to represent the energy consumption of the 3D printer, specifically focusing on the behavior of the stepper motors during printing. The z-axis and extruder motor energy consumption were assumed to be relatively small, therefore the focus was solely on the x-axis and y-axis since they directly relate to toolpath planning. The model considered relevant parameters and the asymmetric movement and loads of the stepper motor [x-axis and y-axis] during printing of each line segment motion. The resulting mathematical model was transformed into a prediction model capable of forecasting stepper motor energy consumption for a given part geometry by directly taking the g-code file as input, eliminating the need for physical experimentation.

When generating a toolpath for 3D printing, the amount of energy consumed by the stepper motors along the x-axis and y-axis can significantly vary depending on the power consumption during different stages of acceleration and coasting. To print a line segment $\overrightarrow{ab}$ shown in Figure 8, the y-axis motor moves a distance of $\overrightarrow{ai}$ while the x-axis motor covers distance $\overrightarrow{ib}$.
Hence, to accurately determine the energy usage for printing a specific line segment $\overrightarrow{ib}$ on the x-axis (a similar procedure applies for the y-axis), it is crucial to consider the time needed for the axis to accelerate, maintain maximum speed while coasting, and decelerate, as well as the corresponding power consumption rates at each stage. Printing a line segment represented by the vector $\overrightarrow{de}$ requires only the x-axis stepper motor to move, while the y-axis stepper motor remains in a holding state, consuming power. Similarly, printing a line segment represented by the vector $\overrightarrow{ef}$ requires only the y-axis stepper motor to move, while the x-axis stepper motor remains in a holding state, consuming power. The time and power consumption rate of the stepper motor in the

holding state are considered in our calculation for each case. These factors play a critical role in determining total energy consumption.

The motion profile for printing a line segment can take either a trapezoidal or triangular shape, as depicted in Figure 9, depending on whether the maximum speed is reached or not. The shaded region on the graph represents the total distance travelled and is equivalent to the length of the line segment. Additionally, it should be emphasized that although the graph displays only positive velocities, the algorithm is configured to account for both positive and negative velocities. To compute the time required for an axis of a line segment to accelerate, coast at maximum speed (if applicable), and decelerate, the following parameters are defined:

- the initial velocity (v_o) of the movement i.e., entry speed.
- the final velocity (v_f) of the movement i.e., exit speed.
- the highest attainable velocity (v_m) that can be achieved for the movement given the constraints on acceleration and jerk.
- the acceleration (a) of the movement (assuming acceleration and deceleration rate are the same)
- the total distance (d) of the movement
- the time taken to accelerate, coast, and decelerate is represented as t_a, t_c, t_d respectively while the time spent in a holding state (i.e., d=0) is represented as t_h
- the power consumption during holding, acceleration, coasting, and deceleration can be represented as $P_h, P_a, P_c, and\ \ P_d\ ,where\ P_d\ = P_a$(assuming negligible friction).

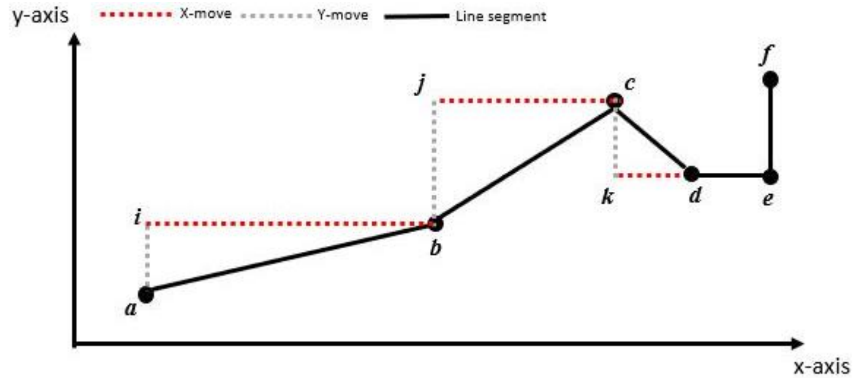

Figure 8. Movement of stepper motors along the x-axis and y-axis to print a line segment.

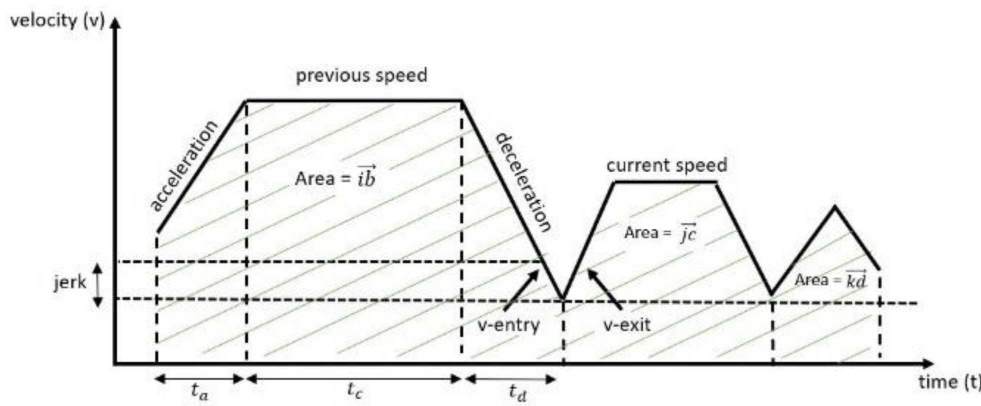

Figure 9. Velocity profile to print line segment along a given x-axis or y-axis.

To find the highest attainable velocity v_m for a given movement, the firmware logic developed by Prusa3d (2017) was adopted which is given as:

Let v_m be represented as current_speed

Let axis length be represented as δ_{mm}

For x – axis

$$\delta_{mm}[X_{AXIS}] = \frac{target[X_{AXIS}] - position[X_{AXIS}]}{cs.axis\_steps\_per\_unit[X_{AXIS}]} \quad (1)$$

For y – axis

$$\delta_{mm}[Y_{AXIS}] = \frac{target[Y_{AXIS}] - position[Y_{AXIS}]}{cs.axis\_steps\_per\_unit[Y_{AXIS}]} \quad (2)$$

The length of a line segment while considering all axis is given as:

$$segment\_length = \sqrt{(\delta_{mm}[X_{AXIS}])^2 + (\delta_{mm}[Y_{AXIS}])^2} \quad (3)$$

The firmware defines nominal_speed as the feed rate, which is the speed at which a stepper motor travels a linear distance measured in millimeters per second. This value is usually programmed together with other motion commands on a line-by-line basis to regulate the printing speed of the toolpath. It is not fixed, and various feed rates may be designated for different sections of the g-code file. Hence, nominal_speed = feed rate

The maximum speed that the stepper motor can achieve in a particular axis is determined by the max feed rate, which is a pre-set limit. Before generating a g-code, this value is established, and any calculated current_speed is adjusted to be within the limit of the max feed rate.

$$time\ taken\ to\ complete\ segment\_length = \frac{segment\_length}{\text{feed rate}} \quad (4)$$

$$current\_speed[i] = \frac{\delta_{mm}[i]}{time\ taken\ to\ complete\ segment\_length} \quad (5)$$

[i] represents either x or y-axis of a line segment.

As mentioned earlier, the value of $current\_speed$ (v_m) is updated based on the conditions below.

IF $current\_speed[i]$ > max feed rate:

THEN $current\_speed[i]$ = max feed rate

ELSE $current\_speed[i]$ is the same.

To find the initial velocity (v_o) and final velocity (v_f) of the movement i.e., entry speed and exit speed respectively:

According to the firmware design and logic the entry speed of a given line segment is the same as the exit speed of the previous line segment for a given axis i.e.

$$v_{o,i} = v_{f,i-1} \quad (6)$$

The initial velocity (v_o) is calculated following these guidelines:

- Limit the junction velocity between two axis line segments to their minimum.
- Choose the lower nominal speed between the two axis line segments, as it is not desirable to attain a higher speed at the junction during coasting for both line segments.
- Calculate the jerk depending on whether the axis is coasting in the same direction or reversing a direction.
- Calculate the velocity factor derived from the jerk calculation and update the junction velocity with the velocity factor.
- The updated junction velocity will be compared to an allowable velocity calculation and the lowest of these two values will be the entry speed (v_o) as shown in Equation 8.

$$v_{allowable} = \sqrt{current\_speed[axis]^2 - 2 \cdot acceleration \cdot \delta_{mm}[axis]} \quad (7)$$

$$v_{entry\_speed} = \min(v_{max\_junction}, v_{allowable}) \quad (8)$$

A detailed description of the mathematical logic summarized in the guidelines above is found in Appendix A.

For a given line segment,

$$distance = \frac{{v_m}^2 - {v_o}^2}{2 * a} \quad (9)$$

If distance < d then maximum speed will be reached, then.

$$t_a = \frac{v_m - v_o}{a}\ ,\ t_c = \frac{d - distance}{v_m}\ ,\ t_d = \frac{v_m - v_f}{a} \quad (10)$$

$$t_i \; occurs \; when \; d \; = \; 0$$

The time taken to accelerate, coast and decelerate to complete the line segment is expressed as:

$$t_T = t_a + t_c + t_d \tag{11}$$

$$E_T = (P_a \cdot t_a) + (P_c \cdot t_c) + (P_a \cdot t_d) \; + \; (P_h \cdot t_h) \tag{12}$$

$$E_T = E_a + E_d \; + E_h \tag{13}$$

If maximum speed will not be reached i.e., if distance ≥ d , the energy taken to accelerate and decelerate to complete the line segment is expressed as:

$$t_a = \frac{v_m - v_o}{a} \; , t_d = \frac{v_m - v_f}{a} \tag{14}$$

$$t_T = t_a + t_{d \, +} \, t_h \tag{15}$$

$$E_{axis} = (P_a \cdot t_a) + (P_d \cdot t_d) + \; (P_h \cdot t_h) \tag{16}$$

$$E_T = E_a + E_d \; + E_h \tag{17}$$

The formula for the theoretical power output of a stepper motor during translation (linear motion) depends on several factors, including the linear speed of the motor, the force required to move the load, and the mechanical efficiency of the system (Acarnley, 2007, p. 81).

$$Power = Torque \times velocity \tag{18}$$

Which can be further represented as:

$$Power = inertia \times acceleration \times arm \times velocity \tag{19}$$

arm represents the distance of the from the pivot point at which the torque is applied (this is a constant).

Efficiency refers to the ability of a system to convert input energy into useful output energy. In the context of a stepper motor, efficiency is a measure of how well the motor can convert electrical energy into mechanical motion. A perfect stepper motor would have 100% efficiency, with no losses due to friction, mechanical inefficiencies, or electrical losses in the coils or driver circuit. However, achieving perfect efficiency in a real-world stepper motor is not possible, and the actual efficiency will depend on a variety of factors such as speed, acceleration, load, and motor characteristics. Mathematical models and simulations can be used to approximate the behavior of stepper motors, but these models can be complex and computationally expensive.

In the present research, a linear model was used to approximate the power consumption of the stepper motors. The efficiency of the motors was assumed to be constant and not to change over time. Other forms of losses, such as friction and mechanical inefficiencies as well as the arm constant, were factored into the calculation of power and energy consumption for the x-axis and y-axis stepper motors (denoted as k_a and k_c) in Equation 20 and 21 respectively.

$$P_{a,j} = k_a v_j m_j a_j, j \in (X, Y) \tag{20}$$

$$P_{c,j} = k_c v_j, j \in (X, Y) \tag{21}$$

Where, k_a is a constant assumed factor for both x-axis and y axis.

m_j represents the inertial mass of the FDM machine for each of the horizontal motion axis, this value is influenced by the kinematic design of the FDM machine, and the part being built during printing. For the FDM machine used in this work, m_y is greater than m_x and it increases throughout the printing process.

The total energy consumption of a printer can be calculated by summing up the energy consumption of all subsystems.

$$E_{x\_y\_total} = \sum_{i=0}^{n} \sum_{j \in (X,Y)} [\frac{t_{a,i} k_a m_j a_j (v_{j,0} + v_{j,m})}{2} + t_{c,i} k_c v_{j,m} + \frac{t_{d,i} k_a m_j a_j (v_{j,m} + v_{j,f})}{2} + \ t_{h,i} k_h \ ] \tag{22}$$

This approach aimed to minimize $E_{x\_y\_total}$ by changing toolpath and part geometry orientation.

Experiments and Analysis

To adopt this energy model for experiments and analysis, four unknowns k_a , m_j, k_c, and k_h were presented with all other parameters obtainable from the g-code file:

- m_j represents the inertia mass on the motor, with m_x for the x-axis and m_y for the y-axis.
- k_a represents an acceleration energy factor (same as deceleration) for the x-axis and y-axis stepper motor.
- k_c represent a coasting energy factor for the x-axis and y-axis stepper motor.
- k_h represent a holding energy factor for the x-axis and y-axis stepper motor (i.e., $d = 0$)

From the information above, the energy model can be further simplified into Equation 23.

$$E_{x\_y\_total} = k_a m_x A + k_a m_y B + \ k_c \mathrm{C} + k_h H \tag{23}$$

where:

A = velocity and time parameters which characterize the x-axis stepper motor behavior while accelerating/decelerating.

B = velocity and time parameters which characterize the y-axis stepper motor behavior while accelerating/decelerating.

C = velocity and time parameters which characterize both the x-axis and y-axis stepper motor behavior while coasting.

H = time parameters which characterize both the x-axis and y-axis stepper motor behavior while holding.

These definitions can be expressed mathematically as:

$$A = \sum_{i=0}^{n} \sum_{j\in(X)} [\frac{t_{a,i}a_j(v_{j,0} + v_{j,m})}{2} + \frac{t_{d,i}a_j(v_{j,m} + v_{j,f})}{2}] \quad (24)$$

$$B = \sum_{i=0}^{n} \sum_{j\in(Y)} [\frac{t_{a,i}a_j(v_{j,0} + v_{j,m})}{2} + \frac{t_{d,i}a_j(v_{j,m} + v_{j,f})}{2}] \quad (25)$$

$$C = \sum_{i=0}^{n} \sum_{j\in(X,Y)} t_{c,i}v_j \quad (26)$$

$$H = \sum_{i=0}^{n} \sum_{j\in(X,Y)} t_{h,i} \quad (27)$$

Variables A, B, C, and H were calculated by going through all the line segment moves in the toolpath obtainable in a g-code file. The unknowns $k_a m_x$, $k_a m_y$, k_c , and k_h presented above were derived from experimental findings through the experimental setup in Table 3 by applying linear regression analysis. The analysis was done with ten observations and four variables (A, B, C, and H) to predict an outcome variable (energy consumption in Watts-hour). The multiple R value is 0.999460 indicating a strong positive correlation between the variables. The R-squared value is 0.9989, which suggests that 99.9% of the variability in the outcome variable is explained by the predictors. The coefficients of variables A, B, C, and H are 0.134857071, 0.131575661, 69.14025683, and 832.7358875, respectively. The result output indicates that the regression is statistically significant with an F-value of 1388.569474 and a p-value of 8.48532 E-08 (refer to Appendix B). The coefficients of a, b, c, and h are represented by $k_a m_x$, $k_a m_y$, k_c , and k_h

respectively. These coefficients were used in the Energy equation shown in Equation 28. It should be noted that we conducted three iterations of our experimental setup to determine the energy factors. This was done to ensure the accuracy and validity of the energy data measurements obtained.

$$E_{x\_y\_total} = 0.134857071A + 0.131575661B + 69.14025683C + 832.7358875H \qquad (28)$$

After deriving the energy model, experiments were carried out to examine the effect of geometry, toolpath pattern type, and orientation on energy consumption. The experiments involved testing five various part geometry shapes (Square, Rectangle, Triangle, Tear drop, and Oval) as illustrated in Figure 10, in conjunction with five different toolpath pattern types. The experimental setup is summarized in Table 4.

Table 3. Table Showing experimental setup to derive energy factors for A, B, C, and H

Geometry	**Infill - Angle**	**A**	**B**	**C**	**H**	**Energy (Wms)**
F shape	Rectilinear 0 degrees	1305994.223	5761881.996	19472.347	653.99	2876745.836
F shape	Rectilinear 90 degrees	1522699.712	6080275.434	19190.296	662.440	2861145.493
L shape	Arch.Chords* 45 degrees	3992591.510	2815755.988	22599.900	11.431	2575507.792
L shape	Concentric 90 degrees	1229483.470	1313570.860	19521.784	483.57	2154690.352
L shape	Rectilinear 0 degrees	1013710.498	1254719.498	19401.187	565.490	2093936.952
L shape	Rectilinear 45 degrees	1541855.921	1726330.135	26971.310	28.120	2178449.241
L shape	Rectilinear 90 degrees	1220885.328	1062564.242	19309.720	565.460	2124597.877
L shape	Octogram Spiral 0 degrees	1597103.263	1703435.373	20938.720	333.710	2267012.829
K shape	Rectilinear 0 degrees	3139631.276	2924868.583	14521.407	549.190	2167387.206
K shape	Rectilinear 90 degrees	2585547.187	3072301.165	14264.401	522.430	2134053.756

Table 4. Experiment setup to derive the total number of runs to be conducted.

S/N	Factor	No of Level	Level Description
1	Geometry	5	Square, Rectangle, Triangle, Tear drop, Oval
2	Toolpath pattern	5	Rectilinear, Concentric, Hilbert Curve, Archimedean Chords, Octogram Spiral
3	Infill Orientation Angle	3	0-degree, 45-degree, 90-degree
4	Geometry Orientation Angle	4	0-degree, 30-degree, 60-degree, 90-degree

Other information includes Infill density: 20%; Layer height: 0.1 mm; First layer height: 0.2mm; Total number of layers: 20.

A factorial Design of Experiments (DOE) with a total number of 300 (= 5 x 5 x 3 x 4) experimental runs was planned.

By utilizing the energy model, these experiments were conducted to gain valuable insights and inform the development of strategies. Information regarding the results is described in Appendix C.

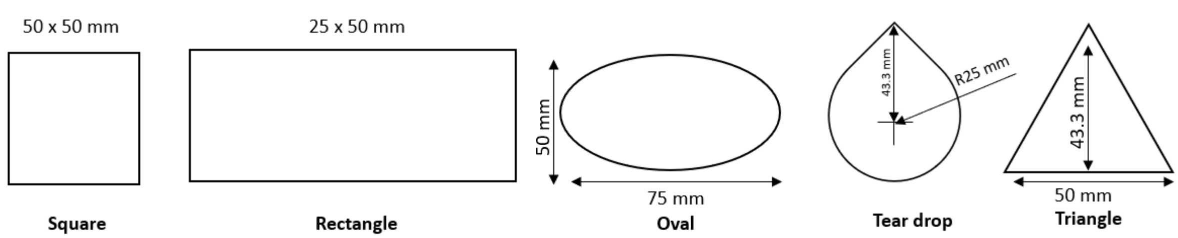

Figure 10. Five distinct part geometry types used in experiments conducted.

CHAPTER 4

RESULTS AND DISCUSSION

The study investigates how the energy consumption of axis stepper motors is affected by varying part geometry, toolpath pattern type, and toolpath orientation. These differences arise from changes in the stepper motor's characteristics, such as acceleration, coasting, and deceleration, as it attempts to print specific line segment motions, resulting in higher energy demand. Appendix D summarizes the results of a subset of the experiments conducted, which focuses on the rectangular geometry print with a constant part geometry orientation and constant toolpath pattern orientation, as depicted in Figure 11 and 12. Note that the energy consumption of the x-axis (E_x) and y-axis (E_y) was calculated using the derived mathematical energy model instead of physical prints.

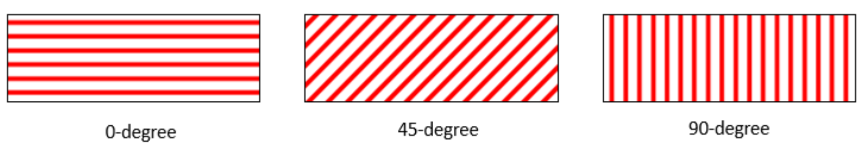

Figure 11. Different orientations (0, 45, and 90 degrees) of a rectilinear toolpath pattern for a rectangular part geometry

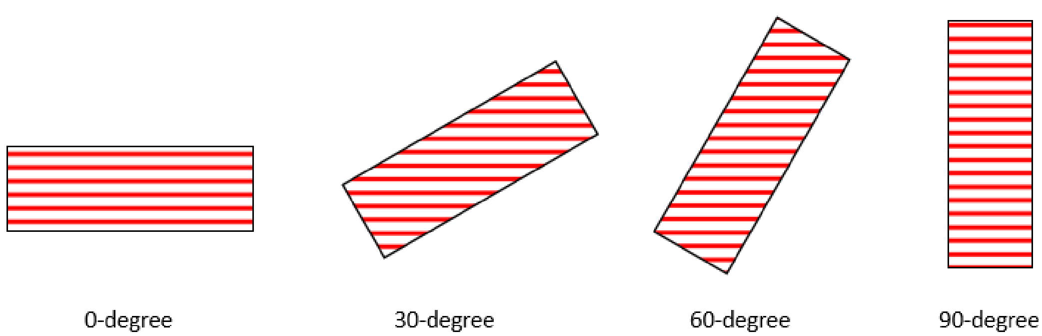

Figure 12. Different orientations (0, 30, 60, and 90 degrees) of a rectangular geometry for a rectilinear toolpath pattern inclined at 0-degree

The experimental results of the scenarios depicted in Figure 11 indicated that orienting the toolpath at 90-degrees minimizes energy consumption regardless of the pattern type selection. In contrast, if the part geometry selection is oriented at 0-degree, the energy consumed is minimized for all toolpath patterns except the Archimedean Chord pattern. However, for any given toolpath pattern type, orienting the toolpath pattern and part geometry at 45-degrees results in a higher energy consumption value.

The experiment conducted also yielded another important finding: the amount of time that stepper motors spend on acceleration/ deceleration has a substantial effect on the energy consumed during printing, in comparison to the time spent coasting. A longer acceleration/ deceleration time results in higher energy consumption, which highlights the need to minimize this occurrence to achieve energy savings. Overall, the insights obtained have led to the development of a toolpath planning strategy for 3D printing, which is as follows:

1. The toolpath for 3D printing should be designed in a way that maximizes the time spent by stepper motors in coasting, while minimizing the time spent in accelerating and decelerating. By considering this aspect when planning the toolpath, it is possible to reduce energy consumption during printing.
2. The angle at which the toolpath is printed can significantly impact energy consumption. Therefore, it is important to choose the toolpath orientation carefully. Based on experiments, it is recommended to avoid printing with the toolpath inclined at a 45-degree angle if minimizing energy consumption is a priority, regardless of the toolpath pattern selection.
3. The choice of toolpath pattern can also affect energy consumption during printing. Experiments have shown that printing with varying toolpath patterns results in varying levels

of energy consumption. This is because certain toolpath pattern types such as Hilbert curve or Archimedean chords contain many short lines segment motions, which increase the time spent by the motor in accelerating and decelerating as compared to coasting. In general, regardless of the orientation of the part geometry, using the rectilinear toolpath pattern type for printing resulted in the lowest energy consumption value among the five toolpath pattern types employed in this research.

4. The orientation of the part geometry being printed can also impact energy consumption by the stepper motors. Therefore, it is essential to consider the part geometry orientation when planning the toolpath. From experiments, the x-axis and y-axis stepper motors do not always consume equal amounts of energy due to the asymmetricity of the x-axis and y-axis inertia masses. The geometry orientation affects the nature of the toolpath and the moves covered by the x-axis and y-axis stepper motors.
5. he variation in toolpath pattern type and toolpath orientation has a greater impact on energy consumption during printing compared to the orientation of the part geometry. An equal degree of change in both toolpath orientation and geometry orientation does not lead to an equivalent change in energy consumption. This crucial observation should be considered when designing a toolpath.

Case Study

Figure 13 illustrates the remodeling of an Engineering bracket that was originally designed by Ferriera de Moraes (2016), to validate the strategies presented earlier.

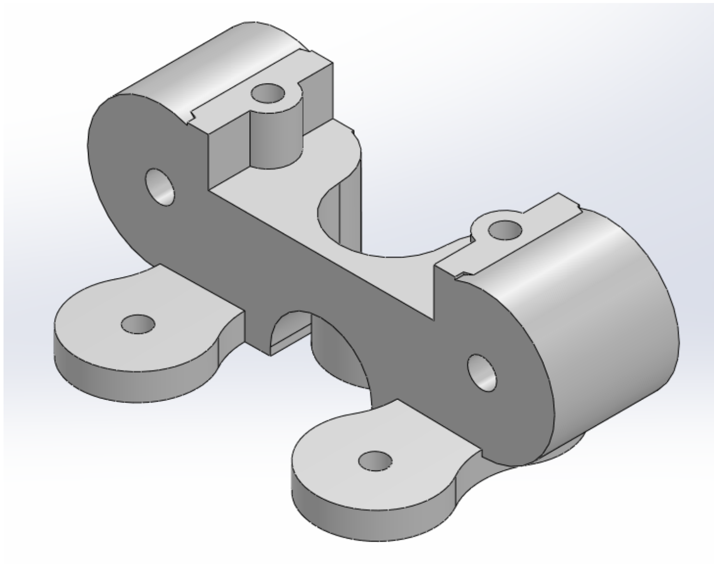

Figure 13. Engineering bracket used for case study analysis.

Following the design of the part, it underwent multiple iterations for printing with the aim of identifying the version that would minimize energy consumption. To achieve this, the experimental setup involved altering the part geometry orientation, toolpath pattern type, and toolpath orientation, as shown in Figure 14. The outcomes of this study, which provide validation for the earlier stated strategy, are documented in Appendix E. The findings are also succinctly summarized using the clustered column charts presented in Figure 15 and 16. In particular, Figure 15 demonstrates the impact of changing the part geometry orientation on energy consumption, revealing that aligning the part at 0-degree (i.e., aligning its longest side with the x-axis) minimizes energy consumption regardless of the chosen toolpath pattern (except for Archimedean Chords pattern). This finding supports the earlier outlined strategy. On the other hand, orienting the part at 45-degree leads to a significant increase in energy consumption during printing.

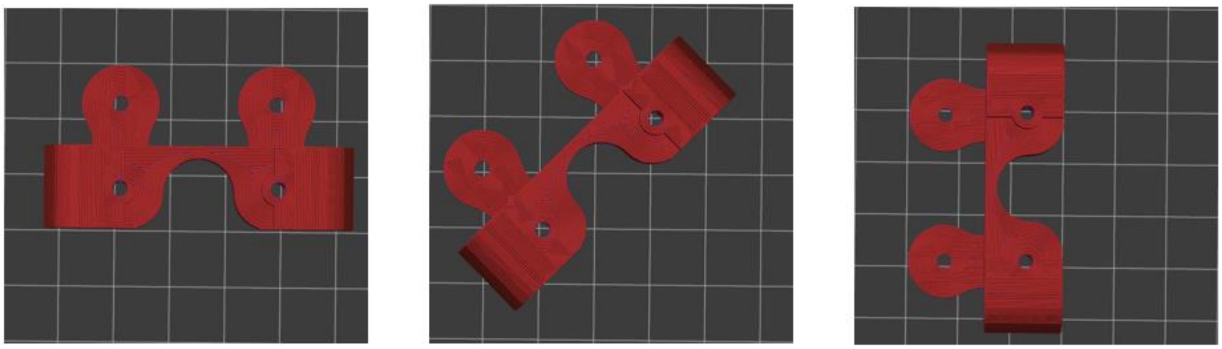

Figure 14. Different orientations (0, 45, and 90 degrees) of the case study part for a 0-degree concentric toolpath pattern

Based on Figure 16, it can be observed that rotating the toolpath pattern by 90 degrees results in lower energy consumption for all patterns except the Archimedean Chords pattern. On the other hand, re-orienting the toolpath pattern by 45 degrees, as described in Figure 11, results in increased energy consumption during printing. In general, the analysis of the geometrical and toolpath pattern undertaken in this study highlights the rectilinear toolpath pattern type as the most effective for minimizing energy consumption in the X and Y axis stepper motors.

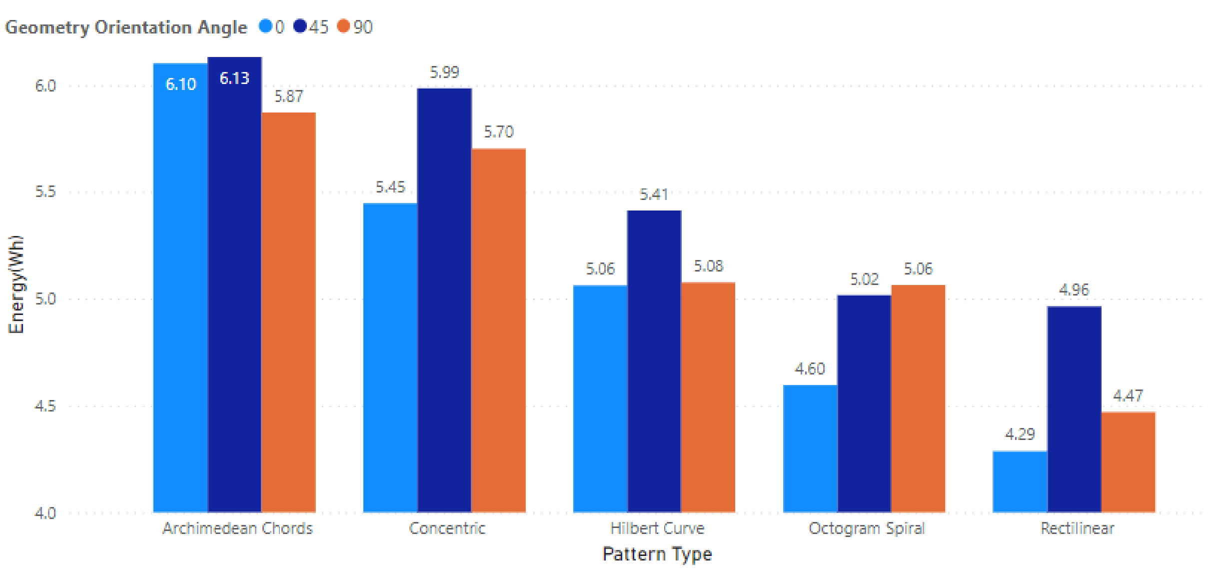

Figure 15. Case study: The effect of orienting part geometry on energy consumption.

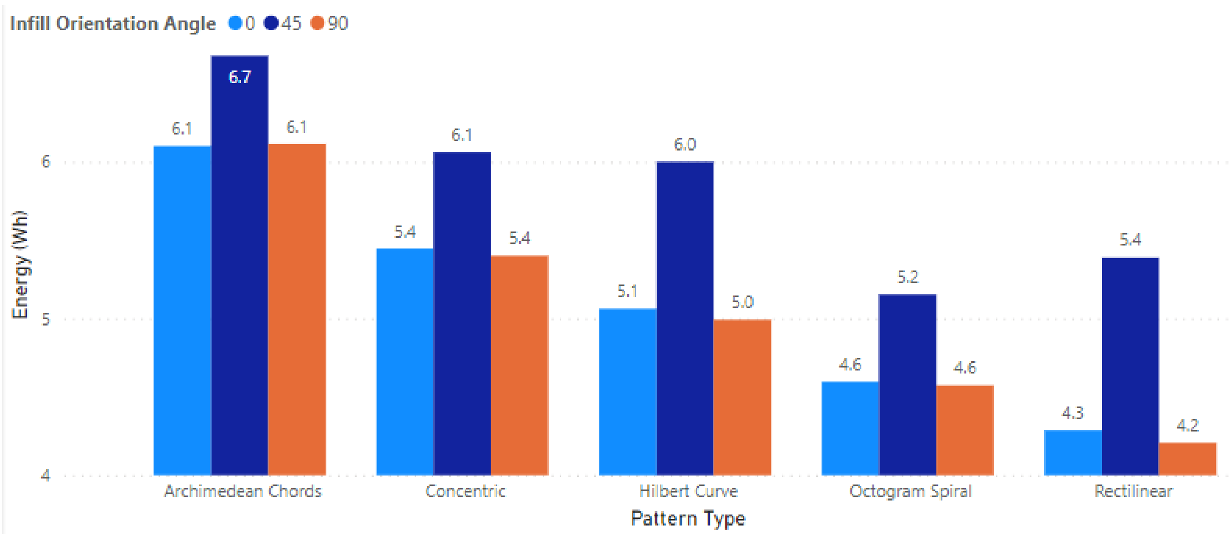

Figure 16. Case study: The effect of orienting toolpath on energy consumption.

CHAPTER 5
CONCLUSION

Notably, the overall energy consumption of a stepper motor is influenced by a variety of factors, such as the motor's construction and design, the driver circuit employed, and the load being moved. The motor's performance can be considerably affected by electrical and mechanical losses. However, the study's focus was solely on exploring the correlation between energy consumption and toolpath. The experiments conducted in this study assumed constant voltage and frequency for the power supply conditions, with a fixed efficiency factor. Future improvements should aim to enhance the precision of energy results while also incorporating the impact of the aforementioned factors on the mathematical model representing the stepper motor's behavior.

The results of the experiments conducted demonstrate that the asymmetric movement of motors during toolpath printing can have a considerable impact on energy consumption. Therefore, aligning the part geometry strategically before printing is crucial to minimize motor energy consumption along the x-axis and y-axis. The energy consumed during printing is a significant factor that should be considered with other factors such as part strength and quality. The initial stages of achieving this goal involve developing models and predicting energy consumption These findings serve as a foundation for future research, which will aim to enhance existing models and propose more efficient toolpath formulation for specific geometrical designs on a layer-by-layer basis, all while taking part quality into account. This research will be especially valuable for larger 3D printers, which require more power to operate, as well as for prints that may last for several days. Additionally, the results f this study have implications for various industries such as aerospace, maritime, and industrial sectors. The findings may pave the way for the creation of techniques to 3D print efficiently in scenarios where energy supply is limited, like space travel or submarines.

REFERENCES

Acarnley, P. (2007). *Stepping motors: a guide to theory and practice 4th edition.* London: The Institution of Engineering and Technology.

Ajay, J., Song, C., Rathore, A. S., Zhou, C., & Xu, W. (2017). 3DGates: An instruction-level energy analysis and optimization of 3d printers. *Proceedings of the Twenty-Second International Conference on Architectural Support for Programming Languages and Operating Systems*, *52*, pp. 419-433.

Azapagic, A., & Perdan, S. (2000). Indicators of Sustainable Development for Industry: A General Framework. *Process Safety and Environmental Protection, 78*(4), 243-261.

Basile, V., Modica, F., Fontana, G., Ruggeri, S., & Fassi, I. (2020). Improvements in accuracy of fused deposition modeling via Integration of low-cost on-board vision systems. *Journal of Micro and Nano-Manufacturing*, 1-5.

Baumers, M., Dickens, P., Tuck, C. J., & Hague, R. J. (2016). The cost of additive manufacturing: machine productivity, economies of scale and technology-push. *Technological Forecasting and Social Change, 102*(5), 193-201.

Baumers, M., Tuck, C. J., Bourell, D., & Sreenivasan, R. (2011). Sustainability of additive manufacturing: Measuring the energy consumption of the laser sintering process. *Proceedings of the Institution of Mechanical Engineers Part B Journal of Engineering Manufacture, 225*(12), 2228-2239.

Bourhis, F. L., Kerbrat, O., Dembinski, L., Hascoet, J., & Mognol, P. (2014). Predictive model for environmental assessment in additive manufacturing process. *Procedia CIRP*, *15*, 26-31.

Castelino, K., D'Souza, R., & Wright, P. K. (2004). Tool-path optimization for minimizing airtime during machining. *Journal of Manufacturing Systems, 22*(3), 173-180.

Chen, D., Heyer, S., Ibbotson, S., Salontis, K., Steingrímsson, J. G., & Thiede, S. (2015). Direct digital manufacturing: definition, evolution, and sustainability implications. *Journal of Cleaner Production*, *107*, 615-625.

Drizo, A., & Pegna, J. (2006). Environmental impacts of rapid prototyping: an overview of research to date. *Raoid Prototyping Journal, 12*(2), 64-71.

Ferriera de Moraes, L. F. (2016, October 23). *Gut feeling bracket - 2.65 Cubic inches - 0,0956lb.* Retrieved March 2023, from GRABCAD COMMUNITY: https://grabcad.com/library/gut-feeling-bracket-2-65-cubic-inches-0-0956lb-1

Flashforge. (2022, September 1). *Why FDM 3D printing becomes the most popular print type?* Retrieved November 4, 2022, from FlashForge 3d Printer: https://www.flashforge.com/news-detail/why-FDM-3d-printing-the-most-popular

Fleming, C., Walker, S., Branyan, C., Nicolai, A., Hollinger, G., & Mengüç, Y. (2017). Toolpath planning for continuous extrusion additive manufacturing. *S3PM*.

Ford, S., & Despeisse, M. (2016). Additive manufacturing and sustainability: an exploratory study of the advantages and challenges. *Journal of Cleaner Production, 137*, 1573-1587.

Formlabs. (2022). *Additive Manufacturing: Industry trends and outlook.* Retrieved November 4, 2022, from formlabs: https://formlabs.com/blog/additive-manufacturing/

Formlabs. (2022). *Additive Manufacturing: Industry Trends and Outlook.* Retrieved November 4, 2022, from formlabs: https://formlabs.com/blog/additive-manufacturing/

Franco, A., Lanzetta, M., & Romoli, L. (2010). Experimental analysis of selective laser sintering of polyamide powders: An energy perspective. *Journal of Cleaner Production, 18*(16), 1722-1730.

Fysikopoulos, A., Papacharalampopoulos, A., Pastras, G., Stavropoulos, P., & Chryssolouris, G. (2013). Energy Efficiency of Manufacturing Processes: A Critical Review. *Procedia CIRP, 7*, 628-633.

Gardan, N., & Schneider, A. (2015). Topological optimization of internal patterns and support in additive manufacturing. *Journal of Manufacturing Systems, 37*, 417-425.

Gokan, M., Marco, T., Vittal, P. V., & Barletta, I. (2013). Energy Related Key Performance Indicators–State of the Art, Gaps and Industrial Needs. *APMS 2013 International Conference. 414*, pp. 257-267. PA, USA: Springer Berlin Heidelberg.

Gupta, P., Krishnamoorthy, B., & Dreifus, G. (2020). Continuous toolpath planning in a graphical framework for sparse infill additive manufacturing. *Computer-Aided Design*, 102880.

Huang, S. H., Liu, P., Mokasdar, A., & Hou, L. (2013). Additive manufacturing and its societal impact: a literature review. *The International Journal of Advanced Manufacturing Technology, 67*, 1191-1203.

Jerry, A., Chen, S., Aditya, S. R., Chi, Z., & Wenyao, X. (2017). 3DGates: An Instruction-Level Energy Analysis and Optimization of 3D Printers. *Proceedings of the Twenty-Second International Conference on Architectural Support for Programming Languages and Operating Systems, 52*, pp. 419-433.

Jin, Y.-a., He, Y., Fu, J.-z., Gan, W.-f., & Lin, Z.-w. (2014). Optimization of tool-path generation for material extrusion-based additive manufacturing technology. *Additive Manufacturing*(1-4), 32-47.

John, J., Devjani, D., Ali, S., Abdallah, S., & Pervaiz, S. (2022). Optimization of 3D printed polylactic acid structures with different infill patterns using Taguchi-grey relational analysis. *Advanced Industrial and Engineering Polymer Research, 37*, 417-425.

Kakaraparthia, S., Tatara, R. A., & Chen, N. (2022). A new boundary interlock geometry design pattern to strengthen FDM part multi-material interface. *Manufacturing Letters, 33*, 664-669.

Kellens, K., Dewulf, W., Overcash, M., & Hauschild, M. Z. (2012). Methodology for systematic analysis and improvement of manufacturing unit process life-cycle inventory (UPLCI)-CO2PE! initiative (cooperative effort on process emissions in manufacturing). Part 1: Methodology description. *International Journal of Life Cycle Assessment*, *17*(1), 69-78.

Kellens, K., Dewulf, W., Overcash, M., & Hauschild, M. Z. (2014). Environmental impact modeling of selective laser sintering processes. *Rapid Prototyping Journal, 20*(6), 459-470.

Kim, M. K., Lee, I. H., & Kim, H.-C. (2018). Effect of fabrication parameters on surface roughness of FDM parts. *International Journal of Precision Engineering and Manufacturing, 19*(1), 137-142.

Kun, K. (2016). Reconstruction and development of a 3D printer using FDM technology. *Procedia Engineering, 149*, 203-211.

Li, Y., Linke, B. S., Voet, H., Falk, B., Schmitt, R., & Lam, M. (2017). Cost, sustainability and surface roughness quality – A comprehensive analysis of products made with personal 3D printers. *CIRP Journal of Manufacturing Science and Technology, 16*, 1-11.

May, G., Taisch, M., Prabhu, V. V., & Barletta, I. (2013). Energy related key performance Indicators–state of the art, gaps and industrial needs. *APMS 2013 International Conference. 414*, pp. 257-267. PA, USA: Springer Berlin Heidelberg.

Meteyer, S., Xu, X., Perry, N., & Zhao, Y. F. (2014). Energy and material flow analysis of binder-jetting additive manufacturing processes. *Procedia CIRP*, *15*(9), 19-25.

Mognol, P., Lepicart, D., & Perry, N. (2006). Rapid prototyping: Energy and environment in the spotlight. *Rapid Prototyping Journal, 12*(1), 26-34.

Munoz, A. A., & Sheng, P. (1995). An analytical approach for determining the environmental impact of machining processes. *Journal of Materials Processing Technology, 53*(3-4), 736-758.

Nguyen, N. D., Ashraf, I., & Kim, W. (2021). Compact model for 3D printer energy estimation and practical energy-saving strategy. *Electronics, 10*(4), 483.

Ong, M. H., Wagner, H., Tuck, C. J., & Hague, R. J. (2008). Body-fitting customisation of motorcycle seats: an investigation of consumer requirements. *International Journal of Mass Customisation, 2*(3-4), 375-393.

Panda, S. K., Padhee, S., & Sood, A. K. (2009). Optimization of fused deposition modelling (FDM) process parameters using bacterial foraging technique. *Intelligent Information Management, 1*(2), 89-97. Retrieved 11 4, 2022

Paul, R., & Anand, S. (2012). Process energy analysis and optimization in selective laser sintering. *Journal of Manufacturing Systems, 31*(4), 429-437.

Peng, T. (2016). Analysis of energy utilization in 3D printing processes. *Procedia CIRP, 40*, 62-67.

Peng, T., & Yan, F. (2018). Dual-objective analysis for desktop FDM printers: Energy consumption and surface roughness. *Procedia CIRP, 69*, 106-111.

Prusa3d. (2017, March 29). *Prusa-Firmware/planner.cpp.* Retrieved September 2022, from GitHub: https://github.com/prusa3d/Prusa-Firmware/blob/6dbf35f6e6b7e5dcaab0f869b2d159b45acc6ba9/Firmware/planner.cpp

Prusa3d. (n.d). *Infill patterns*. Retrieved November 4, 2022, from Prusa3d: https://help.prusa3d.com/article/infill-patterns_177130

Ribeiro, M., Carneiro, O. S., Silva, & Ferreira da Silva, A. (2018). Interface geometries in 3D multi-material prints by fused filament fabrication. *Rapid Prototyping Journal, 25*(1), 38-46.

Ruffo, M., & Hague, R. (2007). Cost estimation for rapid manufacturing- simultaneous production of mixed components using laser sintering. *Proceedings of the Institution of Mechanical Engineers, Part B: Journal of Engineering Manufacture, 221*(11), 1585-1591.

Santos, A. L., Almeida, H. D., Bartolo, H. G., & Bartolo, P. J. (2012). A decision tool for green manufacturing while utilizing additive process. *11th Biennial Conference on Engineering Systems Design and Analysis.* Nantes. France: ESDA 2012.

Short, D. B., Badger, P., Sirinterlikci, A., & B, A. (2015). Environmental health and safety issues in rapid prototyping. *Rapid Prototyping Journal, 21*(1), 105-110.

Sikdar, S. K. (2003). Sustainable development and sustainability metrics. *AIChE Journal, 49*(8), 1928 - 1932.

Sinishaw, G. Y., Bantyirga, B., & Abebe, K. (2021). Analysis of smart grid technology application for power distribution system reliability enhancement: A case study on Bahir Dar power distribution. *Scientific African, 12,* e00840.

Sreenivasan, R., Goel, A., & Bourell, D. L. (2009). Sustainability study in selective laser sintering - An energy perspective. *20th Annual International Solid Freeform Fabrication Symposium, SFF 2009*.

Sreenivasan, R., Goel, A., & Bourell, D. L. (2010). Sustainability issues in laser-based additive manufacturing. *Physics Procedia, 5*, 81-90.

Strano, G., Hao, L., Everson, R., & Evans, K. E. (2011). Multi-objective optimization of selective laser sintering processes for surface quality and energy saving. *Proceedings of the Institution of Mechanical Engineers Part B Journal of Engineering Manufacture, 225*(9), 1673-1682.

Sulaymon, T. A., Petri, H. T., & Rayko, T. (2022). Towards a complex geometry manufacturing: A case study on metal 3D printing of topology optimised bicycle parts with lattices. *IFAC-PapersOnLine, 55*(10), 1515-1520.

Tan, D. K., Maniruzzaman, M., & Nokhodchi, A. (2018). Advanced pharmaceutical applications of hot-melt extrusion coupled with fused deposition modelling (FDM) 3D printing for personalised drug delivery. *Pharmaceutics, 10*(4), 203. doi:10.3390/pharmaceutics10040203

Tuck, C. J., Hague, R., Ruffo, M., & Ransley, M. (2008). Rapid manufacturing facilitated customization. *International Journal of Computer Integrated Manufacturing, 21*(3), 245-258.

Volpato, N., Nakashima, R. T., Galvao, L. C., Barboza, A. O., Benevides, L. C., & Nunes, L. F. (2014). Reducing repositioning distances in fused deposition-based processes using optimization algorithms. *6th International Conference on Advanced Research in Virtual and Rapid Prototyping.* Leiria, Portugal.

Wah, P. K., Murty, K. G., Joneja, A., & Chiu, L. C. (2002). Tool path optimization in layered manufacturing. *IIE Transactions, 34*(4), 335-347.

Walls, S., Corney, J. R., & Vasantha, G. V. (2014). Relative energy consumption of low-cost 3d printers. *The 12 th International Conference on Manufacturing Research.* Southampton, UK: ICMR2014.

Warburg, B. (2018). *Additive manufacturing vs. traditional manufacturing.* Retrieved November 3, 2022, from Animal Ventures: https://blog.animalventures.com/blog/additive-manufacturing-vs-traditional-manufacturing/#:~:text=Additive%20manufacturing%20operates%20by%20adding,to%20create%20the%20desired%20shape.

Weissman, A., & Gupta, S. K. (2011). Selecting a design-stage energy estimation approach for manufacturing processes. *Proceedings of the ASME Design Engineering Technical Conference.*

Weller, C., Kleer, R., & Piller, F. T. (2015). Economic Implications of 3D printing: Market structure models in light of additive manufacturing revisited. *International Journal of Production Economics, 164*, 43-56.

Wohlers, T. (2016). *Wohlers report 2016.* Colorado: Wohlers Associates, Inc.

Wojcik, M., Koszalka, L., Pozniak-Koszalka, I., & Kasprzak, A. (2015). MZZ-GA algorithm for solving path optimization in 3D printing. *ICONS 2015: The Tenth International Conference on Systems*.

Wong, K. V., & Hernandez, A. (2012). A review of additive manufacturing. *ISRN Mechanical Engineering*(4). doi:http://dx.doi.org/10.5402/2012/208760

Xie, J., Liu, F., & Qiu, H. (2016). An integrated model for predicting the specific energy consumption of manufacturing processes. *The International Journal of Advanced Manufacturing Technology, 85*(5-8), 1339-1346.

Xu, X., Meteyer, S., Perry, N., & Zhao, Y. F. (2014). Energy consumption model of binder-jetting additive manufacturing processes. *International Journal of Production Research*, 1-11.

Yang, Y., Li, L., Pan, Y., & Sun, Z. (2017). Energy consumption modeling of stereolithography-based additive manufacturing toward environmental sustainability. *Journal of Industrial Ecology, 21*(4), 168-178. doi:10.1111/jiec.12589

APPENDIX A

DETAILED DESCRIPTION OF THE MATHEMATICAL LOGIC OF ENERGY MODEL TO FIND THE ENTRY SPEED OF A LINE SEGMENT.

Mathematical equation to limit the junction velocity to their minimum (calculating entry speed)
$prev\_speed\_larger$ is **TRUE** $when$ $previous\_nominal\_speed > current\_nominal\_speed$
else its **FALSE**
Next we calculate smaller_speed_factor:

If smaller_speed_factor = $prev\_speed\_larger$ then $\frac{nominal\_speed}{previous\_nominal\_speed}$
Else smaller_speed_factor = $\frac{previous\_nominal\_speed}{nominal\_speed}$
Next we pick the smaller of the nominal speeds compared because we don't want to achieve higher speed at the junction during coasting for the two line segments
If previous_nominal_speed > nominal_speed, then $v_{max\_junction}$ = nominal_speed
else $v_{max\_junction}$ = previous_nominal_speed

Next we calculate entry_speed of a line axis given parameters from the previous line of similar axis
Initiate v_{factor}= 1
Initiate limited = FALSE
We want to limit the jerk in all axes. Looping through the axis:
For axis=[X,Y,Z,E]
Start loop
$v_{exit} = previous\_speed[axis]$
$v_{entry} = current\_speed[axis]$
if (prev_speed_larger) i.e. if $previous\_nominal\_speed > current\_nominal\_speed$
$v_{exit} = v_{exit} \cdot smaller\_speed\_factor$
$v_{exit} = v_{exit} \cdot \frac{nominal\_speed}{previous\_nominal\_speed}$
If (limited is true) then
$v_{exit} = v_{exit} \cdot v_{factor}$
$v_{entry} = v_{entry} \cdot v_{factor}$
Note v_{factor} is derived from jerk calculation.
Calculate the jerk depending on whether the axis is coasting in the same direction or reversing a direction.
Compute Jerk based on the following conditions:
<u>Condition 1</u>
If $v_{exit} > v_{entry}$ and $v_{entry} > 0$ or $v_{exit} < 0$, then
Jerk = $v_{exit} - v_{entry}$ (when coasting)
Jerk = $max(v_{exit}, - v_{entry})$ (when reversing)
<u>Condition 2</u>

If $v_{exit} \leq v_{entry}$ and $v_{entry} < 0$ or $v_{exit} > 0$, then
Jerk = $v_{entry} - v_{exit}$ (when coasting)
Jerk = $max(-v_{exit}, -v_{entry})$ (when reversing)

Given the conditions above,
if $(jerk > cs.max\_jerk[axis])$

$v_{factor} = v_{factor} \cdot \frac{cs.max\_jerk[axis]}{jerk}$

Set limited = TRUE
End loop

If (limited) i.e. when limited is set to TRUE
$v_{max\_junction} = v_{max\_junction} \cdot v_{factor}$
$v_{allowable} = \sqrt{current\_speed[axis]^2 - 2 \cdot acceleration \cdot millimeters}$
$v_{entry\_speed} = \min(v_{max\_junction}, v_{allowable})$.
v_{entry_speed} is the calculated entry speed for the current line axis and exit speed for the previous line axis

APPENDIX B

SUMMARY STATISTICS OF LINEAR REGRESSION ANALYSIS

Summary Statistics of Linear Regression Analysis to find a, b, c, and h

SUMMARY OUTPUT

Regression Statistics	
Multiple R	0.999460313
R Square	0.998920917
Adjusted R Square	0.831714709
Standard Error	100152.934
Observations	10

ANOVA

	df	*SS*	*MS*	*F*	*Significance F*
Regression	4	5.57128E+13	1.39282E+13	1388.569474	8.48532E-08
Residual	6	60183661129	10030610188		
Total	10	5.5773E+13			

	Coefficients	*Standard Error*	*t Stat*	*P-value*	*Lower 95%*	*Upper 95%*	*Lower 95.0%*	*Upper 95.0%*
Intercept	0	#N/A	#N/A	#N/A	#N/A	#N/A	#N/A	#N/A
a	0.134857071	0.031872769	4.231106183	0.005493424	0.056867214	0.212846928	0.056867214	0.212846928
b	0.131575661	0.021151509	6.220627679	0.000797385	0.079819783	0.183331538	0.079819783	0.183331538
c	69.14025683	3.979053804	17.37605477	2.32894E-06	59.40386292	78.87665074	59.40386292	78.87665074
txy_hold	832.7358875	134.8706114	6.17433167	0.000829514	502.71939	1162.752385	502.71939	1162.752385

APPENDIX C

EXPERIMENTAL RESULTS OF DESIGN OF EXPERIMENTS WITH 300 TOTAL RUNS

Experimental results for square geometry

Geometry	Pattern Type	Infill Orientation Angle	Geometry Orientation	Energy(Wms)	Energy(Wh)
Square	Rectilinear	0	0	10817213.1	3.004781416
Square	Rectilinear	0	30	11112641.47	3.086844854
Square	Rectilinear	0	60	11137768.42	3.093824561
Square	Rectilinear	0	90	10817213.1	3.004781416
Square	Rectilinear	45	0	12195544.48	3.387651245
Square	Rectilinear	45	30	12155880.18	3.376633383
Square	Rectilinear	45	60	12156965.91	3.376934975
Square	Rectilinear	45	90	12195544.48	3.387651245
Square	Rectilinear	90	0	10774364.15	2.99287893
Square	Rectilinear	90	30	11078450.97	3.077347491
Square	Rectilinear	90	60	11079189.45	3.077552625
Square	Rectilinear	90	90	10774364.15	2.99287893
Square	Concentric	0	0	10821650.71	3.006014085
Square	Concentric	0	30	11044452.31	3.067903421
Square	Concentric	0	60	11100713.78	3.083531605
Square	Concentric	0	90	10819484.53	3.005412368
Square	Concentric	45	0	12201039.52	3.389177644
Square	Concentric	45	30	12109681.14	3.363800317
Square	Concentric	45	60	12158725.59	3.377423775
Square	Concentric	45	90	12193381.52	3.387050423
Square	Concentric	90	0	10787646.14	2.996568373
Square	Concentric	90	30	11078450.97	3.077347491
Square	Concentric	90	60	11079189.45	3.077552625
Square	Concentric	90	90	10774364.15	2.99287893
Square	Hilbert Curve	0	0	10929718.03	3.036032787
Square	Hilbert Curve	0	30	11214584.59	3.115162385
Square	Hilbert Curve	0	60	11254083.39	3.126134275
Square	Hilbert Curve	0	90	10929718.03	3.036032787
Square	Hilbert Curve	45	0	12321225.53	3.422562648
Square	Hilbert Curve	45	30	12295532.04	3.415425565
Square	Hilbert Curve	45	60	12295118.41	3.415310668
Square	Hilbert Curve	45	90	12321225.53	3.422562648
Square	Hilbert Curve	90	0	10889324.61	3.024812391
Square	Hilbert Curve	90	30	11117431.37	3.088175382
Square	Hilbert Curve	90	60	11152090	3.097802777
Square	Hilbert Curve	90	90	10889324.61	3.024812391

Square	Archimedean Chords	0	0	10411114.48	2.891976243
Square	Archimedean Chords	0	30	10651778.3	2.958827306
Square	Archimedean Chords	0	60	10668763.11	2.963545307
Square	Archimedean Chords	0	90	10411114.48	2.891976243
Square	Archimedean Chords	45	0	11797865.43	3.277184841
Square	Archimedean Chords	45	30	11725441.08	3.257066965
Square	Archimedean Chords	45	60	11734083.53	3.259467649
Square	Archimedean Chords	45	90	11797865.43	3.277184841
Square	Archimedean Chords	90	0	10377763.48	2.882712077
Square	Archimedean Chords	90	30	10614551.39	2.948486497
Square	Archimedean Chords	90	60	10592576.28	2.942382301
Square	Archimedean Chords	90	90	10377763.48	2.882712077
Square	Octogram Spiral	0	0	10960855.22	3.044682005
Square	Octogram Spiral	0	30	11225978.76	3.118327434
Square	Octogram Spiral	0	60	11249979.92	3.124994423
Square	Octogram Spiral	0	90	10960855.22	3.044682005
Square	Octogram Spiral	45	0	12342490.57	3.428469604
Square	Octogram Spiral	45	30	12299339.5	3.416483194
Square	Octogram Spiral	45	60	12301331.35	3.417036486
Square	Octogram Spiral	45	90	12342490.57	3.428469604
Square	Octogram Spiral	90	0	10921952.19	3.033875609
Square	Octogram Spiral	90	30	11178353.44	3.105098178
Square	Octogram Spiral	90	60	11175941.42	3.104428172
Square	Octogram Spiral	90	90	10921952.19	3.033875609

Experimental results for rectangular geometry

Geometry	Pattern Type	Infill Orientation Angle	Geometry Orientation	Energy(Wms)	Energy(Wh)
Rectangle	Rectilinear	0	0	8026480.25	2.229577847
Rectangle	Rectilinear	0	30	8628388.023	2.396774451
Rectangle	Rectilinear	0	60	8667755.273	2.407709798
Rectangle	Rectilinear	0	90	8159112.432	2.26642012
Rectangle	Rectilinear	45	0	9334218.62	2.592838506
Rectangle	Rectilinear	45	30	8548067.45	2.374463181
Rectangle	Rectilinear	45	60	8554043.531	2.376123203
Rectangle	Rectilinear	45	90	8079799.756	2.244388821
Rectangle	Rectilinear	90	0	8004892.09	2.223581136
Rectangle	Rectilinear	90	30	8901805.277	2.472723688
Rectangle	Rectilinear	90	60	8932991.043	2.481386401
Rectangle	Rectilinear	90	90	8429723.572	2.341589881
Rectangle	Concentric	0	0	8086478.99	2.246244164
Rectangle	Concentric	0	30	8548067.45	2.374463181
Rectangle	Concentric	0	60	8554043.531	2.376123203
Rectangle	Concentric	0	90	8079799.756	2.244388821
Rectangle	Concentric	45	0	9328487.38	2.591246494
Rectangle	Concentric	45	30	8857458.589	2.460405164
Rectangle	Concentric	45	60	8911245.583	2.475345995
Rectangle	Concentric	45	90	8363674.209	2.323242836
Rectangle	Concentric	90	0	8036975.80	2.232493279
Rectangle	Concentric	90	30	8474942.077	2.354150577
Rectangle	Concentric	90	60	8401460.956	2.333739155
Rectangle	Concentric	90	90	8118399.441	2.255110956
Rectangle	Hilbert Curve	0	0	8367562.23	2.324322842
Rectangle	Hilbert Curve	0	30	8901805.277	2.472723688
Rectangle	Hilbert Curve	0	60	8932991.043	2.481386401
Rectangle	Hilbert Curve	0	90	8429723.572	2.341589881
Rectangle	Hilbert Curve	45	0	10471872.76	2.908853545
Rectangle	Hilbert Curve	45	30	8812429.439	2.447897066
Rectangle	Hilbert Curve	45	60	8770604.893	2.436279137
Rectangle	Hilbert Curve	45	90	8153300.234	2.264805621
Rectangle	Hilbert Curve	90	0	8312445.45	2.309012624
Rectangle	Hilbert Curve	90	30	8857458.589	2.460405164

Rectangle	Hilbert Curve	90	60	8911245.583	2.475345995
Rectangle	Hilbert Curve	90	90	8363674.209	2.323242836
Rectangle	Archimedean Chords	0	0	8301856.92	2.306071368
Rectangle	Archimedean Chords	0	30	8812429.439	2.447897066
Rectangle	Archimedean Chords	0	60	8770604.893	2.436279137
Rectangle	Archimedean Chords	0	90	8153300.234	2.264805621
Rectangle	Archimedean Chords	45	0	9532819.53	2.648005424
Rectangle	Archimedean Chords	45	30	9146975.71	2.540826586
Rectangle	Archimedean Chords	45	60	9075040.8	2.520844667
Rectangle	Archimedean Chords	45	90	8952054.858	2.486681905
Rectangle	Archimedean Chords	90	0	8215274.42	2.282020672
Rectangle	Archimedean Chords	90	30	8408324.454	2.335645682
Rectangle	Archimedean Chords	90	60	8160326.009	2.266757225
Rectangle	Archimedean Chords	90	90	7751781.422	2.153272617
Rectangle	Octogram Spiral	0	0	8317076.83	2.310299121
Rectangle	Octogram Spiral	0	30	8857458.589	2.460405164
Rectangle	Octogram Spiral	0	60	8911245.583	2.475345995
Rectangle	Octogram Spiral	0	90	8363674.209	2.323242836
Rectangle	Octogram Spiral	45	0	9575944.24	2.659984511
Rectangle	Octogram Spiral	45	30	9430742.668	2.619650741
Rectangle	Octogram Spiral	45	60	9465205.382	2.629223717
Rectangle	Octogram Spiral	45	90	9483865.11	2.634406975
Rectangle	Octogram Spiral	90	0	8268383.01	2.296773058
Rectangle	Octogram Spiral	90	30	8666568.674	2.407380187
Rectangle	Octogram Spiral	90	60	8576985.852	2.38249607
Rectangle	Octogram Spiral	90	90	8277047.061	2.299179739

Experimental results for triangle geometry

Geometry	Pattern Type	Infill Orientation Angle	Geometry Orientation	Energy(Wms)	Energy(Wh)
Triangle	Rectilinear	0	0	5026906.041	1.396362789
Triangle	Rectilinear	0	30	4949654.125	1.374903924
Triangle	Rectilinear	0	60	5053549.85	1.403763847
Triangle	Rectilinear	0	90	4939811.392	1.372169831
Triangle	Rectilinear	45	0	5400455.773	1.500126604
Triangle	Rectilinear	45	30	5448908.611	1.513585725
Triangle	Rectilinear	45	60	5418817.925	1.505227201
Triangle	Rectilinear	45	90	5447451.238	1.5131809
Triangle	Rectilinear	90	0	4988647.721	1.385735478
Triangle	Rectilinear	90	30	4912528.766	1.364591324
Triangle	Rectilinear	90	60	5000090.784	1.388914107
Triangle	Rectilinear	90	90	4898772.272	1.360770076
Triangle	Concentric	0	0	4987732.847	1.385481347
Triangle	Concentric	0	30	4914313.61	1.365087114
Triangle	Concentric	0	60	5014853.828	1.393014952
Triangle	Concentric	0	90	4895145.795	1.359762721
Triangle	Concentric	45	0	5402751.809	1.500764391
Triangle	Concentric	45	30	5415225.37	1.50422927
Triangle	Concentric	45	60	5428787.105	1.507996418
Triangle	Concentric	45	90	5439248.297	1.510902305
Triangle	Concentric	90	0	4951066.909	1.375296363
Triangle	Concentric	90	30	4850982.146	1.347495041
Triangle	Concentric	90	60	4969646.233	1.380457287
Triangle	Concentric	90	90	4946811.003	1.374114168
Triangle	Hilbert Curve	0	0	4940487.986	1.372357774
Triangle	Hilbert Curve	0	30	5099354.777	1.416487438
Triangle	Hilbert Curve	0	60	5191772.945	1.442159151
Triangle	Hilbert Curve	0	90	5080937.161	1.411371433
Triangle	Hilbert Curve	45	0	5525699.741	1.534916595
Triangle	Hilbert Curve	45	30	5554937.035	1.543038065
Triangle	Hilbert Curve	45	60	5539096.972	1.538638048
Triangle	Hilbert Curve	45	90	5555561.892	1.543211637
Triangle	Hilbert Curve	90	0	5104990.184	1.418052829
Triangle	Hilbert Curve	90	30	5028878.663	1.39691074
Triangle	Hilbert Curve	90	60	5130222.905	1.425061918
Triangle	Hilbert Curve	90	90	4509464.044	1.252628901

Triangle	Archimedean Chords	0	0	4894531.524	1.35959209
Triangle	Archimedean Chords	0	30	4844470.052	1.345686126
Triangle	Archimedean Chords	0	60	4918979.658	1.366383238
Triangle	Archimedean Chords	0	90	4878438.306	1.355121752
Triangle	Archimedean Chords	45	0	5303519.265	1.473199796
Triangle	Archimedean Chords	45	30	5384733.534	1.495759315
Triangle	Archimedean Chords	45	60	5312516.088	1.475698913
Triangle	Archimedean Chords	45	90	5381906.886	1.494974135
Triangle	Archimedean Chords	90	0	4831629.236	1.342119232
Triangle	Archimedean Chords	90	30	4824674.765	1.340187435
Triangle	Archimedean Chords	90	60	4874693.976	1.35408166
Triangle	Archimedean Chords	90	90	4788390.545	1.330108485
Triangle	Octogram Spiral	0	0	5088135.137	1.413370871
Triangle	Octogram Spiral	0	30	5019299.792	1.394249942
Triangle	Octogram Spiral	0	60	5101838.23	1.417177286
Triangle	Octogram Spiral	0	90	5014726.167	1.392979491
Triangle	Octogram Spiral	45	0	5483379.653	1.523161015
Triangle	Octogram Spiral	45	30	5542011.615	1.539447671
Triangle	Octogram Spiral	45	60	5512074.415	1.531131782
Triangle	Octogram Spiral	45	90	5528706.845	1.535751902
Triangle	Octogram Spiral	90	0	5029451.867	1.397069963
Triangle	Octogram Spiral	90	30	4965341.318	1.379261477
Triangle	Octogram Spiral	90	60	5052755.855	1.403543293
Triangle	Octogram Spiral	90	90	4932907.393	1.370252054

Experimental results for drop geometry.

Geometry	Pattern Type	Infill Orientation Angle	Geometry Orientation	Energy(Wms)	Energy(Wh)
Drop	Rectilinear	0	0	9166094.505	2.546137363
Drop	Rectilinear	0	30	9048931.414	2.513592059
Drop	Rectilinear	0	60	9162214.159	2.545059489
Drop	Rectilinear	0	90	9281989.226	2.578330341
Drop	Rectilinear	45	0	10050589.03	2.791830285
Drop	Rectilinear	45	30	10100248.02	2.805624449
Drop	Rectilinear	45	60	10059182.18	2.794217273
Drop	Rectilinear	45	90	9999621.403	2.777672612
Drop	Rectilinear	90	0	9102379.852	2.528438848
Drop	Rectilinear	90	30	8994552.546	2.498486818
Drop	Rectilinear	90	60	9207993.825	2.557776063
Drop	Rectilinear	90	90	9255586.518	2.570996255
Drop	Concentric	0	0	9121361.056	2.533711405
Drop	Concentric	0	30	9011514.438	2.503198455
Drop	Concentric	0	60	9056765.557	2.51576821
Drop	Concentric	0	90	9112612.147	2.531281152
Drop	Concentric	45	0	10073263.66	2.798128795
Drop	Concentric	45	30	10066213.96	2.796170545
Drop	Concentric	45	60	9969603.778	2.769334383
Drop	Concentric	45	90	9873623.591	2.74267322
Drop	Concentric	90	0	9066145.053	2.518373626
Drop	Concentric	90	30	8968354.459	2.491209572
Drop	Concentric	90	60	9051711.365	2.514364268
Drop	Concentric	90	90	9045554.843	2.512654123
Drop	Hilbert Curve	0	0	9256284.532	2.571190148
Drop	Hilbert Curve	0	30	9157829.895	2.543841637
Drop	Hilbert Curve	0	60	9299926.015	2.583312782
Drop	Hilbert Curve	0	90	9372745.129	2.603540314
Drop	Hilbert Curve	45	0	10210808.7	2.83633575
Drop	Hilbert Curve	45	30	10239255.66	2.844237682
Drop	Hilbert Curve	45	60	10189166.47	2.83032402
Drop	Hilbert Curve	45	90	10140078.55	2.816688485
Drop	Hilbert Curve	90	0	9164160.383	2.545600106
Drop	Hilbert Curve	90	30	9073303.697	2.520362138
Drop	Hilbert Curve	90	60	9243812.273	2.567725632
Drop	Hilbert Curve	90	90	9300896.106	2.583582252
Drop	Archimedean Chords	0	0	8769284.788	2.435912441
Drop	Archimedean Chords	0	30	8723558.628	2.42321073
Drop	Archimedean Chords	0	60	8863386.652	2.462051848

Drop	Archimedean Chords	0	90	8998558.812	2.49959967
Drop	Archimedean Chords	45	0	8769284.788	2.435912441
Drop	Archimedean Chords	45	30	8723558.628	2.42321073
Drop	Archimedean Chords	45	60	8863386.652	2.462051848
Drop	Archimedean Chords	45	90	8998558.812	2.49959967
Drop	Archimedean Chords	90	0	8769284.788	2.435912441
Drop	Archimedean Chords	90	30	8723558.628	2.42321073
Drop	Archimedean Chords	90	60	8863386.652	2.462051848
Drop	Archimedean Chords	90	90	8998558.812	2.49959967
Drop	Octogram Spiral	0	0	9286041.838	2.579456066
Drop	Octogram Spiral	0	30	9183427.864	2.550952184
Drop	Octogram Spiral	0	60	9302608.328	2.584057869
Drop	Octogram Spiral	0	90	9405197.767	2.612554935
Drop	Octogram Spiral	45	0	10226315.98	2.840643327
Drop	Octogram Spiral	45	30	10239805.77	2.844390492
Drop	Octogram Spiral	45	60	10194921.42	2.831922615
Drop	Octogram Spiral	45	90	10177533.49	2.827092637
Drop	Octogram Spiral	90	0	9223386.271	2.562051742
Drop	Octogram Spiral	90	30	9156295.66	2.543415461
Drop	Octogram Spiral	90	60	9291557.223	2.580988117
Drop	Octogram Spiral	90	90	9345203.545	2.595889874

Experimental results for oval geometry

Geometry	Pattern Type	Infill Orientation Angle	Geometry Orientation	Energy(Wms)	Energy(Wh)
Oval	Rectilinear	0	0	12992618.8	3.609060778
Oval	Rectilinear	0	30	12952870.77	3.598019659
Oval	Rectilinear	0	60	12878507.27	3.57736313
Oval	Rectilinear	0	90	12836278.45	3.565632903
Oval	Rectilinear	45	0	14201912.65	3.944975737
Oval	Rectilinear	45	30	14229987.29	3.952774246
Oval	Rectilinear	45	60	14261415.92	3.961504423
Oval	Rectilinear	45	90	14238418.61	3.955116281
Oval	Rectilinear	90	0	12949907.36	3.597196488
Oval	Rectilinear	90	30	12947625.87	3.596562742
Oval	Rectilinear	90	60	12855624.83	3.571006898
Oval	Rectilinear	90	90	12785098.54	3.551416261
Oval	Concentric	0	0	12522766.84	3.478546345
Oval	Concentric	0	30	12610389.38	3.50288594
Oval	Concentric	0	60	12637793.03	3.510498063
Oval	Concentric	0	90	12614833.96	3.504120543
Oval	Concentric	45	0	13796313.51	3.832309308
Oval	Concentric	45	30	13910227.18	3.863951995
Oval	Concentric	45	60	14044425.34	3.90122926
Oval	Concentric	45	90	14112292.14	3.92008115
Oval	Concentric	90	0	12474266.73	3.465074091
Oval	Concentric	90	30	12578823.34	3.494117594
Oval	Concentric	90	60	12593543.37	3.498206491
Oval	Concentric	90	90	12572509.47	3.492363741
Oval	Hilbert Curve	0	0	13104646.19	3.640179498
Oval	Hilbert Curve	0	30	13049004.65	3.624723513
Oval	Hilbert Curve	0	60	13064188.3	3.628941193
Oval	Hilbert Curve	0	90	12949292.86	3.597025795
Oval	Hilbert Curve	45	0	14363691.91	3.989914419
Oval	Hilbert Curve	45	30	14427028.05	4.007507791
Oval	Hilbert Curve	45	60	14427048.3	4.007513417
Oval	Hilbert Curve	45	90	14458926.99	4.016368608
Oval	Hilbert Curve	90	0	13040910.25	3.622475069
Oval	Hilbert Curve	90	30	13388424.44	3.719006789
Oval	Hilbert Curve	90	60	13388502.2	3.719028389
Oval	Hilbert Curve	90	90	12901827.28	3.583840912
Oval	Archimedean Chords	0	0	12606590.79	3.501830775

Oval	Archimedean Chords	0	30	12621654.99	3.506015275
Oval	Archimedean Chords	0	60	12382497.44	3.439582622
Oval	Archimedean Chords	0	90	12268743.48	3.407984299
Oval	Archimedean Chords	45	0	13903082.7	3.861967417
Oval	Archimedean Chords	45	30	13889121.34	3.858089262
Oval	Archimedean Chords	45	60	13800126.67	3.833368521
Oval	Archimedean Chords	45	90	13736728.03	3.815757787
Oval	Archimedean Chords	90	0	12525817.42	3.479393728
Oval	Archimedean Chords	90	30	12510241.62	3.475067116
Oval	Archimedean Chords	90	60	12366241.26	3.435067017
Oval	Archimedean Chords	90	90	12201629.17	3.389341436
Oval	Octogram Spiral	0	0	13137031.97	3.649175546
Oval	Octogram Spiral	0	30	13105257.63	3.640349342
Oval	Octogram Spiral	0	60	13025927.07	3.618313075
Oval	Octogram Spiral	0	90	12972756.97	3.603543603
Oval	Octogram Spiral	45	0	14401070.67	4.000297409
Oval	Octogram Spiral	45	30	14426699.79	4.007416608
Oval	Octogram Spiral	45	60	14431177.76	4.00866049
Oval	Octogram Spiral	45	90	14432695.88	4.00908219
Oval	Octogram Spiral	90	0	13070149.18	3.630596996
Oval	Octogram Spiral	90	30	13060000.85	3.627778015
Oval	Octogram Spiral	90	60	12993421.68	3.609283799
Oval	Octogram Spiral	90	90	12934969.75	3.593047153

APPENDIX D

RESULTS OF INFILL AND GEOMETRICAL ORIENTATION ANALYSIS

Infill Orientation Analysis (DOE Subset)

Infill Orientation Angle	Geometry Orientation	tx_acc	tx_coast	tx_decc	tx_hold	ty_acc	ty_coast	ty_decc	ty_hold	t_hold_total	a	b	c	a+b+c	**Energy(Wms)**
0	0	723.51	976.83	840.12	615.19	114.14	411.36	101.93	1046.77	1661.97	2599889.875	8151227.506	75489.80792	10826607.2	8026480.25
45	0	216.91	1352.57	190.37	38.12	210.35	1380.82	178.75	25.93	64.05	7598270.419	7592749.304	104963.196	15295982.9	9334218.62
90	0	838.19	413.31	899.58	1187.73	117.44	983.72	102.03	477.00	1664.74	2744227.154	7642386.775	75830.99261	10462444.9	8004892.088
0	0	727.82	967.92	842.83	636.56	114.76	457.22	101.20	1020.96	1657.52	2690465.536	8162209.494	76213.63487	10928888.7	8086478.99
45	0	198.62	1318.91	177.85	85.35	198.04	1036.81	169.40	391.23	476.58	7539648.914	7414574.335	100365.1117	15054588.4	9328487.377
90	0	728.13	753.04	732.04	847.83	110.18	676.92	95.94	806.38	1654.21	2956369.103	7377316.48	76512.48159	10410198.1	8036975.805
0	0	70.65	627.89	937.26	1089.09	377.20	517.37	263.22	768.52	1857.60	2996239.955	13411022.74	67284.09825	16474546.8	8367562.231
45	0	741.56	1047.79	466.98	31.56	744.30	1234.53	446.52	23.56	55.12	15190092.92	14425597.79	93714.19004	29709404.9	10471872.76
90	0	731.86	398.72	827.37	1312.51	365.52	748.86	254.13	545.08	1857.59	3283997.93	12642492.22	67388.38688	15993878.5	8312445.446
0	0	1240.57	846.23	1282.42	569.73	224.16	778.84	179.78	667.55	1237.28	4997711.032	10367487.66	75693.13437	15440891.8	8301856.923
45	0	715.64	1192.71	609.46	29.24	300.42	1369.03	231.45	27.10	56.34	9867440.227	9448745.202	99970.52176	19416156	9532819.526
90	0	1929.03	625.85	1194.79	790.54	408.66	1005.92	258.00	443.16	1233.70	5244741.97	9342717.004	75952.36888	14663411.3	8215274.42
0	0	780.84	983.84	918.68	616.65	156.88	698.21	210.70	777.79	1394.44	3642596.566	9109646.911	79057.2198	12831300.7	8317076.834
45	0	244.45	1320.59	209.93	74.67	245.02	1285.67	200.72	138.91	213.58	8555121.589	8405235.995	103245.8392	17063603.4	9575944.24
90	0	772.38	757.04	761.27	836.98	155.46	921.66	210.94	556.08	1393.06	3932522.211	8318527.378	79309.64966	12330359.2	8268383.008

Geometrical Orientation Analysis (DOE Subset)

Infill Orientation Angle	Geometry Orientation	tx_acc	tx_coast	tx_decc	tx_hold	ty_acc	ty_coast	ty_decc	ty_hold	t_hold_total	a	b	c	a+b+c	**Energy(Wms)**
0	0	723.511162	976.83	840.12	615.19	114.14	411.36	101.93	1046.77	1661.97	2599889.875	8151227.506	75489.80792	10826607.19	8026480.25
0	30	141.848555	968.18	123.18	593.30	178.04	418.26	147.90	1109.63	1702.93	6293965.868	8933823.054	75007.50308	15302796.43	8628388.023
0	60	209.78993	968.63	655.99	542.21	813.41	414.50	454.33	1158.27	1700.49	8219329.805	7377060.308	74813.4573	15671203.57	8667755.273
0	90	124.216003	979.89	124.43	529.85	70.10	411.18	168.29	1187.90	1717.75	7852459.085	3372928.252	75584.35792	11300971.69	8159112.432
0	0	726.423874	972.25	842.07	631.90	205.83	446.35	147.02	979.69	1611.59	2679088.037	8145188.972	76139.42497	10900416.43	8039329.688
0	30	132.709256	1014.91	113.64	551.51	177.59	799.75	146.66	713.21	1264.71	5974895.144	8897207.966	79815.75167	14951918.86	8548067.45
0	60	200.499387	1012.10	637.50	501.99	813.42	799.52	452.71	755.63	1257.62	7737333.517	7328113.338	79536.03404	15144982.89	8554043.531
0	90	203.182114	688.70	254.86	754.99	66.07	727.43	54.74	866.67	1621.66	7590626.119	3314849.137	76215.80369	10981691.06	8079799.756
0	0	70.6478198	627.89	937.26	1089.09	377.20	517.37	263.22	768.52	1857.60	2996239.955	13411022.74	67284.09825	16474546.8	8367562.231
0	30	143.352892	623.78	216.66	1062.85	425.76	525.98	310.54	813.57	1876.42	6469020.646	14070168.88	66756.42415	20605945.95	8901805.277
0	60	246.127913	621.78	749.62	1012.85	1050.42	523.87	617.33	855.40	1868.25	8290298.08	12565701.84	66616.55206	20922616.47	8932991.043
0	90	120.401059	624.44	206.20	1007.00	313.94	518.83	210.07	886.04	1893.03	7874001.58	8692974.919	67221.02452	16634197.52	8429723.572
0	0	240.569512	846.23	1282.42	569.73	224.16	778.84	179.78	667.55	1237.28	4997711.032	10367487.66	75693.13437	15440891.83	8301856.923
0	30	431.480431	845.71	380.23	551.91	294.96	781.29	227.19	713.41	1265.32	8897369.001	10477228.76	74924.98559	19449522.74	8812429.439
0	60	444.400573	853.83	802.95	501.28	993.70	773.79	583.83	758.44	1259.73	11210985.48	8430342.846	73770.01066	19715098.34	8770604.893
0	90	268.866981	855.62	234.09	487.13	396.71	759.46	291.08	787.51	1274.64	10812797.76	4342685.48	73217.64992	15228700.89	8153300.234
0	0	780.842924	983.84	918.68	616.65	156.88	698.21	210.70	777.79	1394.44	3642596.566	9109646.911	79057.2198	12831300.7	8317076.834
0	30	178.857521	930.86	229.22	639.09	223.07	674.51	183.52	847.73	1486.82	7092750.017	10117295.51	77113.2506	17287158.78	8857458.589
0	60	278.48448	883.18	729.80	642.41	862.51	720.34	485.40	837.14	1479.55	9021594.311	8655633.357	76998.1962	17754225.86	8911245.583
0	90	159.994465	910.77	229.45	601.66	117.12	763.80	85.76	823.32	1424.99	8304860.26	4476005.784	79087.53764	12859953.58	8363674.209

APPENDIX E

RESULTS OF INFILL AND GEOMETRICAL ORIENTATION ANALYSIS (CASE STUDY)

Infill Orientation Analysis (Case Study)

Pattern Type	Geometry Orientation	Infill Orientation	tx_acc	tx_coast	tx_decc	tx_hold	ty_acc	ty_coast	ty_decc	ty_hold	t_hold_total	a	b	c	a+b+c	Energy(Wms)
Rectilinear	0	0	2343.03	2765.50	2168.16	1429.70	1521.05	2415.92	968.99	1709.91	3139.61	15114887	25241939	107835.2	40464661.2	15429798.49
Rectilinear	0	45	2785.67	3381.25	2362.53	404.18	1636.58	3392.67	1140.89	501.17	905.35	33686763	36750900	134007.2	70571670.1	19397627.42
Rectilinear	0	90	2721.03	2661.16	2642.85	1495.22	1353.52	2508.86	864.88	1539.38	3034.60	14195360	24762378	107668.7	39065406.5	15143734.78
Concentric	0	0	5318.11	2532.64	5513.82	1753.27	2220.02	2925.68	1866.54	1694.09	3447.36	25457767	34472402	126783.1	60056952.6	19605449.39
Concentric	0	45	5515.91	2928.45	5662.66	1096.00	2197.39	3382.23	1893.84	1042.18	2138.18	35722075	41950061	140467.1	77812603.3	21829451.46
Concentric	0	90	5327.50	2500.03	5658.70	1776.44	1756.26	2974.51	1631.14	1647.73	3424.17	25051764	33724731	126941.5	58903435.8	19443957.91
Hilbert Curve	0	0	2343.52	2479.44	2251.98	2623.95	3391.75	2280.23	1983.02	2312.03	4935.98	16883700	34561836	105403.4	51550939.5	18222367.8
Hilbert Curve	0	45	3729.22	3560.82	2958.06	310.20	2671.80	3628.02	1779.09	482.70	792.90	43795807	46423509	129147.6	90348463.3	21603948.94
Hilbert Curve	0	90	2626.66	2491.21	2536.73	2615.83	2472.37	2407.65	1568.40	2254.23	4870.05	16507160	32795020	106665.6	49408845.2	17971489.67
Archimedean Chords	0	0	3972.32	3244.57	3501.10	968.49	7094.54	3158.80	3962.47	1155.61	2124.11	28297442	59486813	123693.4	87907948.2	21964142.34
Archimedean Chords	0	45	4090.01	3561.66	3521.80	306.79	2261.87	3748.31	1564.99	482.10	788.89	38722998	66752951	135673.7	105611622	24042583.07
Archimedean Chords	0	90	4964.41	3204.12	4073.39	996.38	6954.50	3346.06	4144.22	1115.51	2111.89	28741989	59187495	124295.9	88053779.9	22016191.74
Octogram Spiral	0	0	2389.26	3040.71	2049.04	1129.13	2387.23	2520.35	1643.32	1806.22	2935.35	21411785	25103373	114418.2	46629576.4	16545799.17
Octogram Spiral	0	45	2489.81	3438.09	2195.82	461.63	1731.42	2971.08	1580.06	1159.56	1621.19	31180319	32068970	126953.2	63376241.8	18551977.49
Octogram Spiral	0	90	2685.48	3027.30	2372.06	1164.21	1531.97	2568.00	1409.55	1779.09	2943.30	20944672	24569362	114977.4	45629011.4	16457828.42

Geometrical Orientation Analysis (Case Study)

Pattern Type	Infill Orientation	Geometry Orientation	tx_acc	tx_coast	tx_decc	tx_hold	ty_acc	ty_coast	ty_decc	ty_hold	t_hold_total	a	b	c	a+b+c	**Energy(Wms)**
Rectilinear	0	0	2343.026	2765.505	2168.158	1429.702	1521.045	2415.921	968.9881	1709.911	3139.612992	15114887	25241939	107835.2	40464661.2	15429798.49
Rectilinear	0	45	1509.625	2882.234	1410.222	1407.529	1460.511	2907.961	1277.37	1170.178	2577.70637	21247520	34753573	119840.1	56120932.9	17870424.15
Rectilinear	0	90	1027.611	2372.479	1137.798	2137.528	2515.81	2803.716	2416.64	1117.613	3255.14178	12739664	29969518	111559.5	42820741.2	16085217.83
Concentric	0	0	5318.105	2532.645	5513.821	1753.271	2220.017	2925.683	1866.542	1694.094	3447.364466	25457767	34472402	126783.1	60056952.6	19605449.39
Concentric	0	45	2978.146	3407.872	2649.953	837.9842	3329.883	3728.648	2605.26	717.0368	1555.020972	33915721	40769426	149178.6	74834324.7	21547208.18
Concentric	0	90	2398.203	2635.182	2665.469	2078.884	5462.706	2926.407	5123.749	1563.741	3642.624948	28264981	35095270	131107.1	63491358.4	20527540.54
Hilbert Curve	0	0	2343.521	2479.444	2251.982	2623.948	3391.751	2280.233	1983.015	2312.031	4935.979099	16883700	34561836	105403.4	51550939.5	18222367.8
Hilbert Curve	0	45	2023.703	2681.653	1758.852	2415.683	2924.905	2846.462	2033.515	1611.27	4026.95229	21064766	40810186	114579.9	61989531.5	19485833.08
Hilbert Curve	0	90	1550.262	2189.115	2841.207	3116.338	2547.82	2480.671	2224.691	1842.38	4958.71801	14788246	36476511	106288.9	51371046.4	18271867.19
Archimedean Chords	0	0	3972.322	3244.571	3501.097	968.4929	7094.541	3158.803	3962.473	1155.613	2124.105441	28297442	59486813	123693.4	87907948.2	21964142.34
Archimedean Chords	0	45	2823.268	3346.878	2310.903	848.1232	3289.812	3599.004	2482.662	732.2313	1580.354493	40317356	48075158	130055.8	88522569.8	22070713.94
Archimedean Chords	0	90	6642.478	3051.351	4396.619	1420.35	3188.74	3500.74	2724.714	797.5045	2217.854721	48579085	33102397	121330.9	81802812.9	21142438.86
Octogram Spiral	0	0	2389.265	3040.709	2049.044	1129.125	2387.227	2520.352	1643.318	1806.223	2935.348492	21411785	25103373	114418.2	46629576.4	16545799.17
Octogram Spiral	0	45	2305.522	2879.632	3324.875	1404.844	3004.683	2943.271	2215.022	1124.07	2528.914517	22354459	35388169	119798.8	57862426.9	18059718.77
Octogram Spiral	0	90	2618.344	2381.581	2390.685	2376.575	2428.147	3194.567	2217.774	880.8578	3257.432824	16265394	38345019	119728.9	54730141.3	18229444.65